JGR Space Physics

RESEARCH ARTICLE
10.1029/2020JA027939

Whole Atmosphere Model Simulations of Ultrafast Kelvin Wave Effects in the Ionosphere and Thermosphere

Y. Yamazaki[1], Y. Miyoshi[2], C. Xiong[1], C. Stolle[1,3], G. Soares[4], and A. Yoshikawa[5]

[1]GFZ German Research Centre for Geosciences, Potsdam, Germany, [2]Department of Earth and Planetary Sciences, Kyushu University, Fukuoka, Japan, [3]Faculty of Science, University of Potsdam, Potsdam, Germany, [4]Observatório Nacional, Rio de Janeiro, Brazil, [5]International Center for Space Weather Science and Education, Kyushu University, Fukuoka, Japan

Key Points:
- GAIA simulations are performed for ultrafast Kelvin wave (UFKW) in the middle and upper atmosphere
- UFKW produces eastward-propagating ~3-day ionospheric variations with zonal wavenumber 1
- First magnetic detection of UFKW in the equatorial electrojet is also presented

Supporting Information:
- Figure S1

Correspondence to:
Y. Yamazaki,
yamazaki@gfz-potsdam.de

Citation:
Yamazaki, Y., Miyoshi, Y., Xiong, C., Stolle, C., Soares, G., & Yoshikawa, A. (2020). Whole atmosphere model simulations of ultra-fast Kelvin wave effects in the ionosphere and thermosphere. *Journal of Geophysical Research: Space Physics*, *125*, e2020JA027939. https://doi.org/10.1029/2020JA027939

Received 21 FEB 2020
Accepted 28 MAY 2020
Accepted article online 11 JUN 2020

©2020. The Authors.
This is an open access article under the terms of the Creative Commons Attribution License, which permits use, distribution and reproduction in any medium, provided the original work is properly cited.

Abstract This paper examines the response of the upper atmosphere to equatorial Kelvin waves with a period of ~3 days, also known as ultrafast Kelvin waves (UFKWs). The whole atmosphere model Ground-to-topside model of Atmosphere and Ionosphere for Aeronomy (GAIA) is used to simulate the UFKW events in the late summer of 2010 and 2011 as well as in the boreal winter of 2012/2013. When the lower layers of the model below 30-km altitude are constrained with meteorological data, GAIA is able to reproduce salient features of the UFKW in the mesosphere and lower thermosphere as observed by the Aura Microwave Limb Sounder. The model also reproduces ionospheric response, as validated through comparisons with total electron content data from the Gravity field and steady-state Ocean Circulation Explorer satellite as well as with earlier observations. Model results suggest that the UFKW produces eastward-propagating ~3-day variations with zonal wavenumber 1 in the equatorial zonal electric field and *F* region plasma density. Model results also suggest that for a ground observer, identifying ionospheric signatures of the UFKW is a challenge because of ~3-day variations due to other sources. This issue can be overcome by combining ground-based measurements from different longitudes. As a demonstration, we analyze ground-based magnetometer data from equatorial stations during the 2011 event. It is shown that wavelet spectra of the magnetic data at different longitudes are only in partial agreement, with or without a ~3-day peak, but a spectrum analysis based on multipoint observations reveals the presence of the UFKW.

1. Introduction

Equatorial Kelvin waves are a type of global-scale waves in the atmosphere. In classical theory (Holton & Lindzen, 1968; Matsuno, 1966), they travel eastward with perturbations in the zonal velocity and geopotential but with no meridional velocity component. The amplitude is largest at the equator, and it decays exponentially with latitude. Equatorial Kelvin waves propagate vertically upward from the source region in the troposphere where they are thought to be excited by latent heating due to tropical convection. They are often classified into three categories according to the wave period (and hence the zonal phase speed): slow Kelvin waves with periods 10–20 days, fast Kelvin waves with periods 5–10 days, and ultrafast Kelvin waves (UFKWs) with periods 2–5 days. In general, a wave with a shorter period and longer wavelength is less susceptible to dissipation and thus is able to reach higher altitudes. As the wave propagates to higher altitudes, it grows in amplitude due to the reduction in atmospheric density. The shortest-period waves, thus UFKWs, can propagate well into the mesosphere and lower thermosphere (MLT) region before being dissipated. Therefore, UFKWs can be a significant source of wave forcing in the upper atmosphere among other global-scale waves such as tides and planetary waves (Liu, 2016; Yiğit & Medvedev, 2015).

Equatorial Kelvin waves were first identified in the lower stratosphere from radiosonde measurements. Wallace and Kousky (1968) found equatorial Kelvin waves with periods ~15 days and vertical wavelength of ~10 km, which are now known as slow Kelvin waves. Hirota (1978, 1979) detected fast Kelvin waves with periods ~10 days and vertical wavelength 15–20 km in the upper stratosphere and lower mesosphere using rocket and satellite measurements. Salby et al. (1984) were the first to observe the UFKW. They found UFKWs with periods ~4 days and vertical wavelength ~40 km in the mesosphere based on the

temperature data from the Nimbus-7 satellite. Lieberman and Riggin (1997) confirmed the presence of UFKWs at altitudes between 65 and 110 km using wind measurements from the UARS satellite. Forbes et al. (2009), using temperature measurements from the SABER instrument on the TIMED satellite, showed a transition of dominant waves from fast Kelvin waves (periods 5–10 days and vertical wavelengths 9–13 km) in the stratosphere to UFKWs (periods 2–3 days and vertical wavelengths 35–45 km) in the MLT region. Their results also showed that for fast Kelvin waves, the zonal wavenumber 1 and zonal wavenumber 2 components are comparable in amplitude, while for UFKWs, the zonal wavenumber 1 component is dominant. Vincent (1993) and subsequent studies (Davis et al., 2012; Pancheva et al., 2004; Riggin et al., 1997; Sridharan et al., 2002; Yoshida et al., 1999) used wind measurements from meteor radars to examine UFKWs in the MLT region. UFKW activity is usually observed in short-lived bursts, which last a few wave cycles. England et al. (2012) and Egito et al. (2018) presented evidence for nonlinear interaction between UFKWs and diurnal tide, which leads to the modulation of the tidal amplitude with UFKW periodicities. Chen et al. (2018) examined the seasonal variability of the UFKW using SABER temperature measurements during 2002–2016, pointing out that the upward propagation of the UFKW is influenced by both the mesospheric and the stratospheric semiannual oscillations. Liu et al. (2019), using a similar data set, examined the interannual variability of the UFKW at 110 km. The observed year-to-year variations were attributed to changes in the solar flux as well as to the quasi-biennial oscillation and El Niño–Southern oscillation of the atmosphere. Gasperini et al. (2015, 2018) used the accelerometer data from the Gravity field and steady-state Ocean Circulation Explorer (GOCE) satellite to detect UFKWs in the thermosphere at ~250-km altitude, which was shown to be consistent with the UFKWs observed in the MLT region at the same time.

Studies have also shown that the UFKW can affect the ionosphere. Takahashi et al. (2006, 2007) observed ~3-day variations in ionospheric parameters (h'F and foF2) and attributed them to the UFKWs simultaneously detected in the MLT region. Liu et al. (2012) examined global maps of total electron content (TEC) and incoherent scatter radar data during the UFKW event of January 2010. They suggested that the observed spatial and temporal features of the ~3-day variations in TEC and electron density are consistent with the modulation of the equatorial plasma fountain by the UFKW. Phanikumar et al. (2014) observed TEC variations with UFKW periodicity (3–5 days) during January–February 2009 and associated them with the major sudden stratospheric warming (SSW) event that took place at this time. Gu et al. (2014) presented observations of UFKWs in the temperature and zonal wind in the MLT region and simultaneously in global TEC maps and COSMIC electron density during the year 2011. They showed that there is a good correspondence between UFKW activity in the MLT region and that in the low-latitude ionosphere. Abdu et al. (2015) pointed out that the equatorial vertical plasma drift velocity at postsunset times sometimes exhibits ~3-day variations during UFKW events in the MLT region.

Numerical models have been used to study excitation, dissipation, and propagation characteristics of the UFKW. Forbes (2000) used a linear mechanistic model, in which UFKWs are generated through theoretical wave forcing (as predicted by classical wave theory) in the lower atmosphere. By running the model with the same wave forcing but with different background winds, it was demonstrated that the distribution of the zonal mean wind at the equator plays an important role for the UFKW propagation into the MLT region. Miyoshi and Fujiwara (2006), using a general circulation model (GCM), showed that the dissipation of UFKWs in the MLT region and accompanying momentum deposition into the mean flow can make a significant contribution to the intraseasonal variation of the zonal mean zonal wind in that region. Chen and Miyahara (2012) investigated fast Kelvin waves and UFKWs generated in a GCM simulation. Both waves showed vertical propagation from the troposphere to higher altitudes, and they dissipate in the MLT region (~60–80 km for the fast Kelvin waves and ~90–110 km for the UFKWs). Chang et al. (2010) used the NCAR Thermosphere Ionosphere Mesosphere Electrodynamics GCM (TIME-GCM) to evaluate the impact of the UFKW on the thermosphere and ionosphere. Theoretical UFKW forcing was applied at the lower boundary of the model at ~30 km. Their results indicated thermospheric mass density perturbations of 8–12% at 350-km altitude and low-latitude TEC perturbations of 25–50% in response to the UFKW that has an amplitude of 20–40 m/s in the zonal wind in the MLT region. They also clarified that the thermospheric response is due to the direct propagation of the wave into the upper thermosphere, while the ionospheric effects are caused by the modulation of the dynamo electric field. Onohara et al. (2013), using an ionospheric wind dynamo model, showed that ~3-day variations in the equatorial vertical plasma drift velocity can be reproduced by forcing the model with a parameterized UFKW and diurnal tide. Sassi et al. (2013), in their

investigation of the January 2009 SSW simulated by the Whole Atmosphere Community Climate Model eXtended version (WACCM-X), noted an enhancement of the UFKW in the MLT region during the SSW. Nystrom et al. (2018), based on a TIME-GCM simulation for April 2009, explained how nonlinear interactions between UFKWs and tides can lead to a rich wave spectrum in the MLT region. Triplett et al. (2019) used the TIE-GCM, which is similar to the TIME-GCM but with the lower boundary at ~97 km. The model was forced with a theoretical UFKW at the lower boundary, which was shown to produce TEC perturbations of ±10% at low latitudes.

The present study also utilizes a numerical model to examine the UFKW in the middle and upper atmosphere. Specifically, we use the whole atmosphere model GAIA, which stands for Ground-to-topside model of Atmosphere and Ionosphere for Aeronomy. The main objectives of this study are to demonstrate the model's ability to reproduce UFKW events that actually occurred in the real atmosphere and to understand the nature of the ionospheric variability caused by the wave activity. In many previous simulations, the UFKW was generated by artificial forcing inserted at a certain height with a fixed oscillation period and zonal wavenumber and with a latitudinal structure of perturbations predicted by linear wave theory (Chang et al., 2010; Forbes, 2000; Onohara et al., 2013; Triplett et al., 2019). An advantage of this approach is that it is able to easily isolate the wave effects by switching on and off the forcing in the model, but the downside is that it is not possible to make a direct comparison with observations for any particular event. Only a few numerical studies used realistic forcing based on meteorological data to drive the UFKW (Nystrom et al., 2018; Sassi et al., 2013). Sassi et al. (2013) were able to reproduce the UFKW observed in the SABER temperature at 100-km altitude during January–February 2009. It needs to be remembered, however, that this was achieved by constraining the WACCM-X for the entire middle and lower atmosphere (0–90 km) with assimilation products. Nystrom et al. (2018) constrained the lower boundary of the TIME-GCM at ~30 km with meteorological reanalysis data for April 2009 and found marked UFKW activity in the MLT region at 90–150 km. However, they did not make a direct comparison with measurements. Therefore, it is uncertain at this point whether numerical models are capable of reproducing the UFKW in the MLT region in response to realistic forcing in the lower atmosphere. Besides, neither Sassi et al. (2013) nor Nystrom et al. (2018) investigated the ionospheric response, which still needs to be validated in the context of whole atmosphere modeling through direct comparisons with observations. This study addresses these issues by the use of the GAIA model and observational data from the middle atmosphere and ionosphere, which are described in the following section. Section 3 presents our results regarding the UFKW in the MLT region and ionosphere. The performance of the model is also evaluated therein. In section 4, we discuss the nature of the ionospheric variability during times of enhanced UFKW activity, based on a case study of the August–September 2011 event. Summary and conclusions are provided in section 5.

2. Model and Data

2.1. GAIA Model

GAIA is a physics-based numerical model of the Earth's whole atmosphere (e.g., Jin et al., 2011; Miyoshi et al., 2011). The model simulates the dynamics, thermodynamics, chemistry, and electrodynamics of the coupled atmosphere-ionosphere system from the surface to the upper thermosphere/ionosphere. GAIA consists of three models that are coupled to one another: a whole atmosphere GCM (Miyoshi & Fujiwara, 2003), an ionosphere model (Shinagawa, 2011), and an electrodynamics model (Jin et al., 2008). The whole atmosphere GCM has the horizontal resolution 2.8° in longitude and latitude and the vertical resolution of a grid per 0.2 scale height, which is sufficient for resolving global-scale waves such as equatorial Kelvin waves and tides. The upper boundary is at 1.017×10^{-9} hPa, which corresponds to 480- to 620-km altitude in our simulations. The ionosphere model has the upper boundary at ~2,000-km altitude. The electron density is derived as a sum of the densities of O^+, O_2^+, N_2^+, and NO^+, and TEC is derived by vertically integrating the electron density. The electrodynamics model solves a wind dynamo equation to calculate electric fields and currents in a tilted dipole magnetic field configuration under the assumption of equipotential magnetic field lines.

The neutral atmosphere below 30 km is constrained with meteorological reanalysis data provided by the Japan Meteorological Agency (Kobayashi et al., 2015; Onogi et al., 2007) using a nudging technique similar to those used by Jin et al. (2012) and Miyoshi et al. (2017). In this way, the model takes into account wave forcing from the lower atmosphere to the upper atmosphere including the ionosphere. The model also

takes into account time-dependent forcing by energetic solar radiation. The daily $F_{10.7}$ index (Tapping, 2013) is used as a proxy of the solar EUV/UV flux, which dominates heating and ionization processes in the upper atmosphere. Geomagnetically quiet conditions are realized by setting the cross polar cap potential to a low and constant value of 30 kV throughout the simulation. Therefore, the day-to-day variability in the model arises from meteorological and solar radiation forcings but not from magnetospheric forcing.

A wave analysis was performed to identify UFKWs and other global-scale waves. At a given latitude, the amplitude A and phase φ of waves with period τ are expressed in the following formula:

$$\sum_{s=-4}^{4} A_s \cos\left[\frac{\Omega}{\tau}t + s\lambda - \Phi_s\right]. \quad (1)$$

Here Ω is the rotation rate of the Earth ($=2\pi$/day), t is the universal time (days), λ is the longitude (radians), and s is the zonal wavenumber. Waves with eastward and westward phase propagations correspond to $s<0$ and $s>0$, respectively, and zonally symmetric oscillations are $s=0$. In the remainder of this paper, eastward- and westward-propagating waves with zonal wavenumber s are also referred to as E$|s|$ and W$|s|$, respectively. For example, the UFKW is eastward propagating with zonal wavenumber $s=-1$ and hence an E1 wave. Standing oscillations are, in this case, denoted as S0. For each day, least squares fitting was performed to GAIA data at a given latitude and height using time windows that are three times the wave period.

2.2. Geopotential Height

The geopotential height (GPH) measurements from the Microwave Limb Sounder (MLS) aboard the Aura satellite (Schwartz et al., 2008; Waters et al., 2006) are used to identify UFKW events as well as to validate UFKWs reproduced by GAIA. Aura is NASA's ongoing satellite mission. The spacecraft was launched into a sun-synchronous low Earth orbit on 15 July 2004. The Aura/MLS provides measurements of GPH profiles for pressure levels from 261 (~9 km) to 0.001 hPa (~97 km). Version 4.2 data (Livesey et al., 2017) during 2004–2019 were obtained from the Goddard Earth Sciences Data and Information Services Center (Acker & Leptoukh, 2007). A wave analysis was performed in a similar way as described for GAIA. The reader is referred to Yamazaki and Matthias (2019) for the detailed description of how the Aura/MLS GPH data were processed for the wave analysis.

It is noted that since the Aura satellite is in a sun-synchronous orbit, the measurements are limited to two local solar times at ~1:45 p.m. and ~1:45 a.m. Therefore, the wave analysis is based on the data at these local times, which contrasts to the wave analysis for GAIA that includes the data from all local times. Nevertheless, we found good agreement between the UFKW derived from GAIA GPH including all local times and that derived from GAIA GPH at local solar times of MLS measurements (i.e., ~1:45 p.m. and ~1:45 a.m.), indicating that the limited local time coverage of Aura/MLS does not necessarily affect its ability to detect UFKWs. This justifies the comparison of UFKWs in GPH from Aura/MLS and GAIA (section 3.1) despite the difference in local time coverage.

2.3. Total Electron Content

TEC data from ESA's GOCE mission are used to evaluate UFKW effects in the ionosphere. The GOCE satellite was launched into a sun-synchronous low Earth orbit on 17 March 2009 and operated in the thermosphere at an altitude of ~250 km until October 2013. The slant TEC was derived from Global Positioning System (GPS) observations and then converted to the vertical TEC (Kervalishvili et al., 2018). The retrieval procedure is similar to that used earlier for deriving TEC from the GPS data for the CHAMP and Swarm satellites (e.g., Noja et al., 2013). A wave analysis was performed separately for the data from the ascending and descending orbital nodes, at ~7 p.m. and ~7 a.m. local solar time, respectively. This is because UFKW effects in the ionosphere are known to be local time dependent (Gu et al., 2014). The wave analysis of GAIA TEC data was also performed separately at each local solar time. The resulting problem of aliasing will be discussed in section 4.1. It is noted that GOCE TEC represents the vertical integration of the plasma density from the height of GOCE (~250 km) to the height of GPS satellites, which differs from TEC measured at ground level. According to GAIA simulations, TEC at 250 km is lower than the ground TEC only by ~10%.

2.4. Geomagnetic Field

Ground-based magnetometer data were obtained from five observatories: Huancayo (12.0°S, 75.3°W), Tatuoca (1.2°S, 48.5°W), Addis Ababa (9.0°N, 38.8°E), Tirunelveli (8.7°N, 77.8°E), and Yap Island (9.3°N, 138.5°E). These observatories are longitudinally apart, but they are all located near the magnetic equator (i.e., within ±3° magnetic latitudes). Magnetic data from Huancayo and Addis Ababa are provided through INTERMAGNET (Love & Chulliat, 2013), while Tirunelveli data are provided by the World Data Center (WDC) for Geomagnetism, Mumbai. The Tatuoca data are provided by Observatório Nacional (Morschhauser et al., 2017) and accessible from GFZ Data Services (Soares, Matzka & Pinheiro 2018). The magnetometer at Yap Island belongs to the global magnetometer network MAGDAS (Yumoto & the MAGDAS Group, 2006), and the data are accessible through SuperMAG (Gjerloev, 2012).

For each station, the magnetic northward (N) component of the geomagnetic field was derived through a coordinate conversion. The data were corrected for magnetic disturbances associated with large-scale magnetospheric currents, such as the ring current and magnetotail current (e.g., Lühr et al., 2017). The correction was performed by subtracting the external field obtained from the magnetic field model CHAOS-6 (Finlay et al., 2016). Furthermore, quiet-day nighttime values were subtracted from the time series of N for each station, which removes the magnetic fields originating from the Earth's core and lithosphere. The residual field ΔN represents magnetic perturbations produced by electric currents in the ionosphere. Since the observatories are close to the magnetic equator, ΔN is dominated by the effect of the equatorial electrojet, which is a narrow band of a zonal current along the magnetic equator (e.g., Yamazaki & Maute, 2017). The equatorial electrojet is closely associated with the equatorial zonal electric field (EEF) generated through wind dynamo processes in the ionospheric *E* region (e.g., Alken, 2020).

3. Results

3.1. UFKWs in the MLT Region

Figure 1 shows the amplitude of the UFKW in GPH at 0.001 hPa (~97 km) in the lower thermosphere during 2004–2019. The UFKW amplitude here is defined as the largest amplitude of the E1 waves within periods of 2.25–3.75 days. The amplitude tends to be largest over the equator, and its latitudinal structure is symmetric about the equator. These features are consistent with those reported earlier by Liu et al. (2019) based on SABER temperature data at 110 km during 2002–2018. There are occasionally bursts of wave activity with amplitudes exceeding 0.2 km at the equator, which is appreciably larger than the typical 1σ error in the amplitude (<0.05 km) estimated by Yamazaki and Matthias (2019). In what follows, we validate the performance of GAIA in reproducing UFKWs in the MLT region. Our focus is on these three events that involve particularly strong UFKW activity: (1) September 2010, (2) August–September 2011, and (3) December 2012–January 2013.

Figure 2 presents wave spectra from $s=-2$ to $s=+2$ at 0.001 hPa (~97 km) over the equator during the September 2010 event. The left panel is derived form the Aura/MLS observations while the right panel is from GAIA simulations. Enhanced wave activity is seen throughout September 2010 for E1 waves with a period around 2.5 days, which can be identified as UFKWs. Other spectral components are mostly on the background level below 0.1 km, except there is some W1 wave activity with a period of 4–7 days at the end of August, which is likely due to the Rossby normal mode, the so-called quasi 6-day wave (e.g., Gan et al., 2018; Gu, Ruan, et al. 2018). In Figures 3 and 4, wave spectra are plotted in a similar format as Figure 2 but for the August–September 2011 event and the December 2012 to January 2013 event, respectively. In either case, the GAIA reproduces the temporal variation of UFKW activity well but with slightly lower amplitudes.

Figures 5a–5d compare the vertical structures of the observed and simulated UFKWs during the August–September 2011 event. The amplitude and phase are derived for the E1 wave with a period of 3.0 days. The GAIA captures the height growth and latitudinal spread of the UFKW amplitude well. The phase structure of the UFKW in the MLT region (above 1 hPa) is also well reproduced by GAIA. Similarly, good agreement is obtained between the Aura/MLS observations and GAIA simulations for the September 2010 event and the December 2012 to January 2013 event. Figures 5e–5h show the model-data comparisons of the UFKW amplitudes for these events. It is noted that the December 2012 to January 2013 event involves three discrete bursts of UFKW activity (Figure 4), and in Figures 5g and 5h, we highlight only the event of 7–15

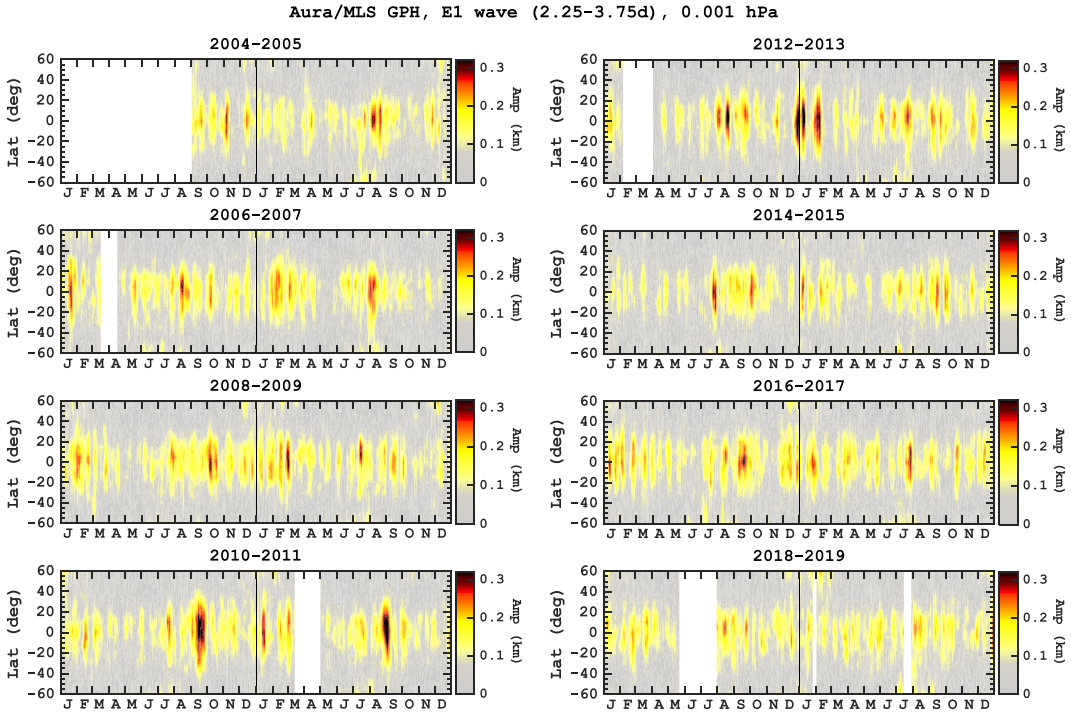

Figure 1. Amplitude of the ultrafast Kelvin wave (UFKW) as derived from the geopotential height (GPH) measurements at 0.001 hPa (~97-km altitude) by the Aura Microwave Limb Sounder during 2004–2019. The UFKW amplitude is defined as the largest amplitude of the eastward-propagating waves with zonal wavenumber 1 within periods of 2.25–3.75 days.

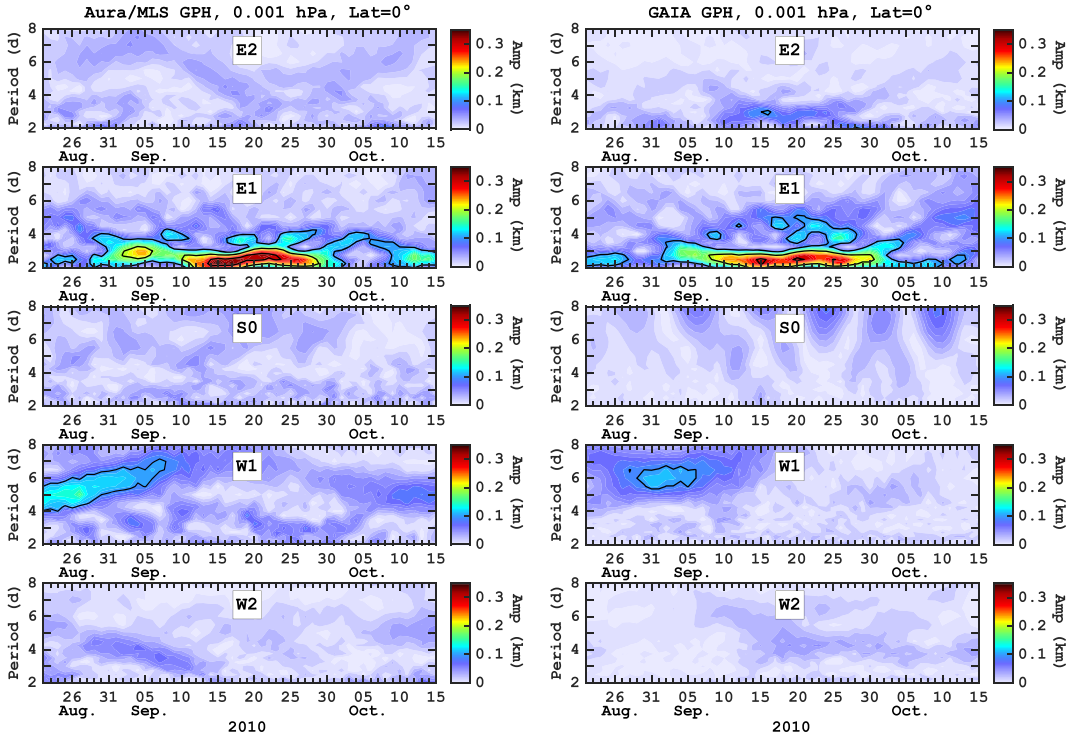

Figure 2. Time versus period diagrams of the wave spectrum derived from the geopotential height (GPH) at 0.001 hPa (~97-km altitude) over the equator for zonal wavenumber $s = -2$ (E2), $s = -1$ (E1), $s = 0$ (S0), $s = +1$ (W1), and $s = +2$ (W2) during the ultrafast Kelvin wave (UFKW) event of September 2010. The left panels are from the Aura Microwave Limb Sounder measurements while the right panels are from the GAIA model.

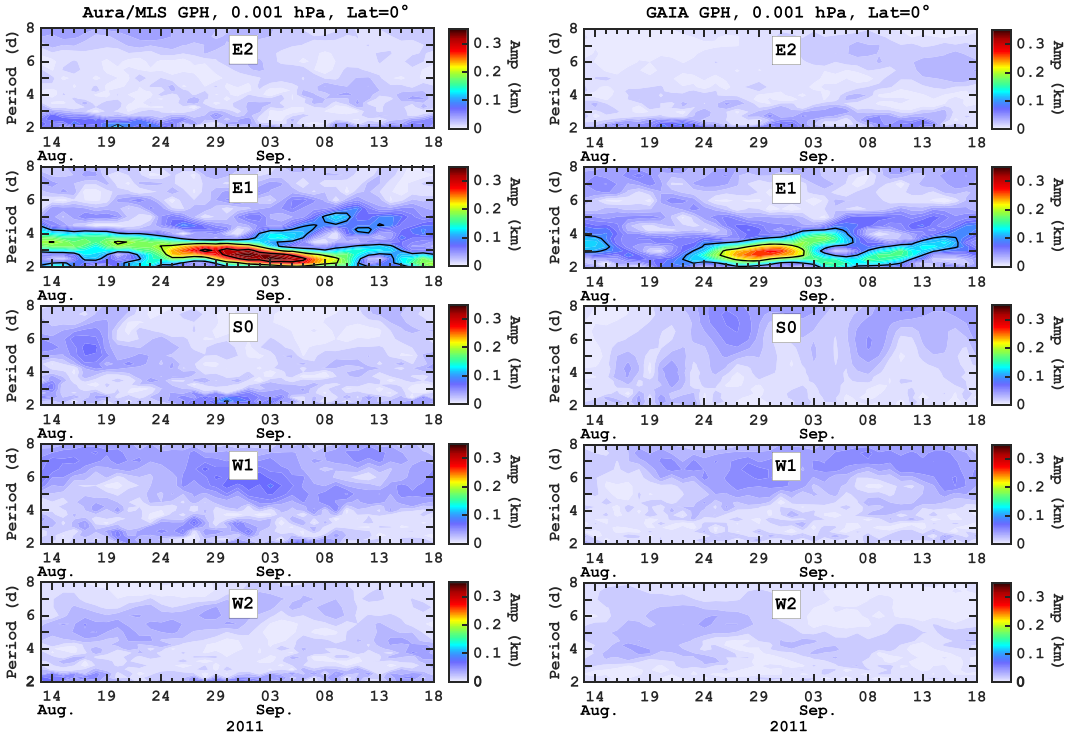

Figure 3. Same as Figure 2 except for the ultrafast Kelvin wave (UFKW) event of August–September 2011.

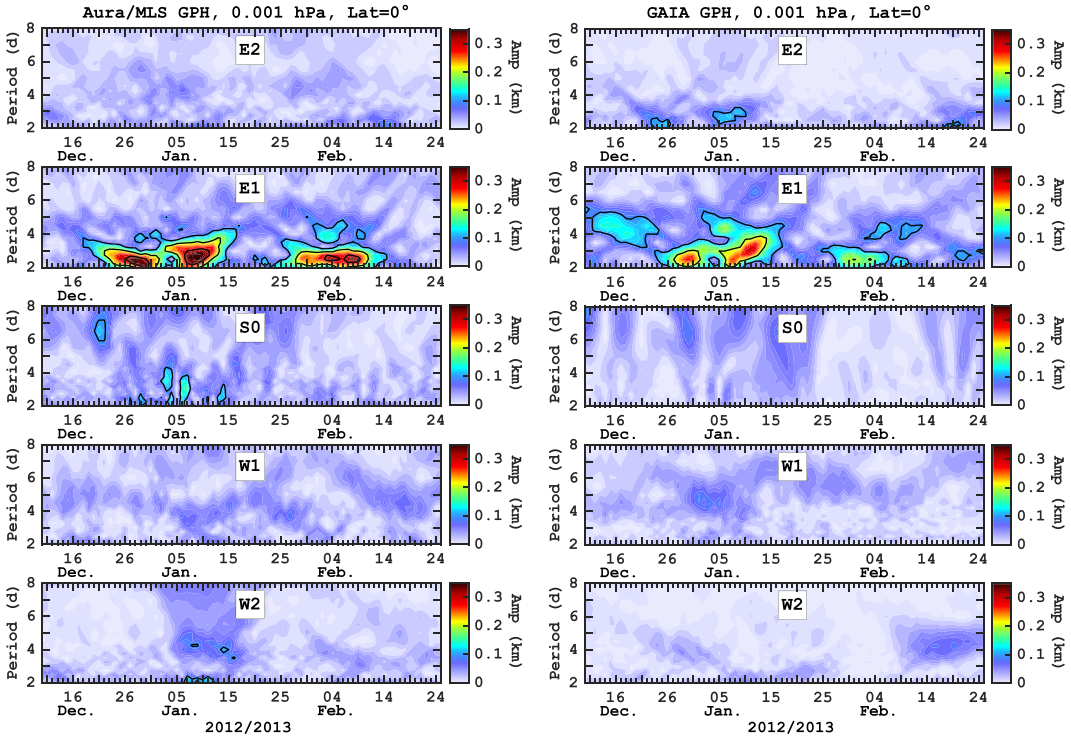

Figure 4. Same as Figure 2 except for the ultrafast Kelvin wave (UFKW) event of December 2012 to January 2013.

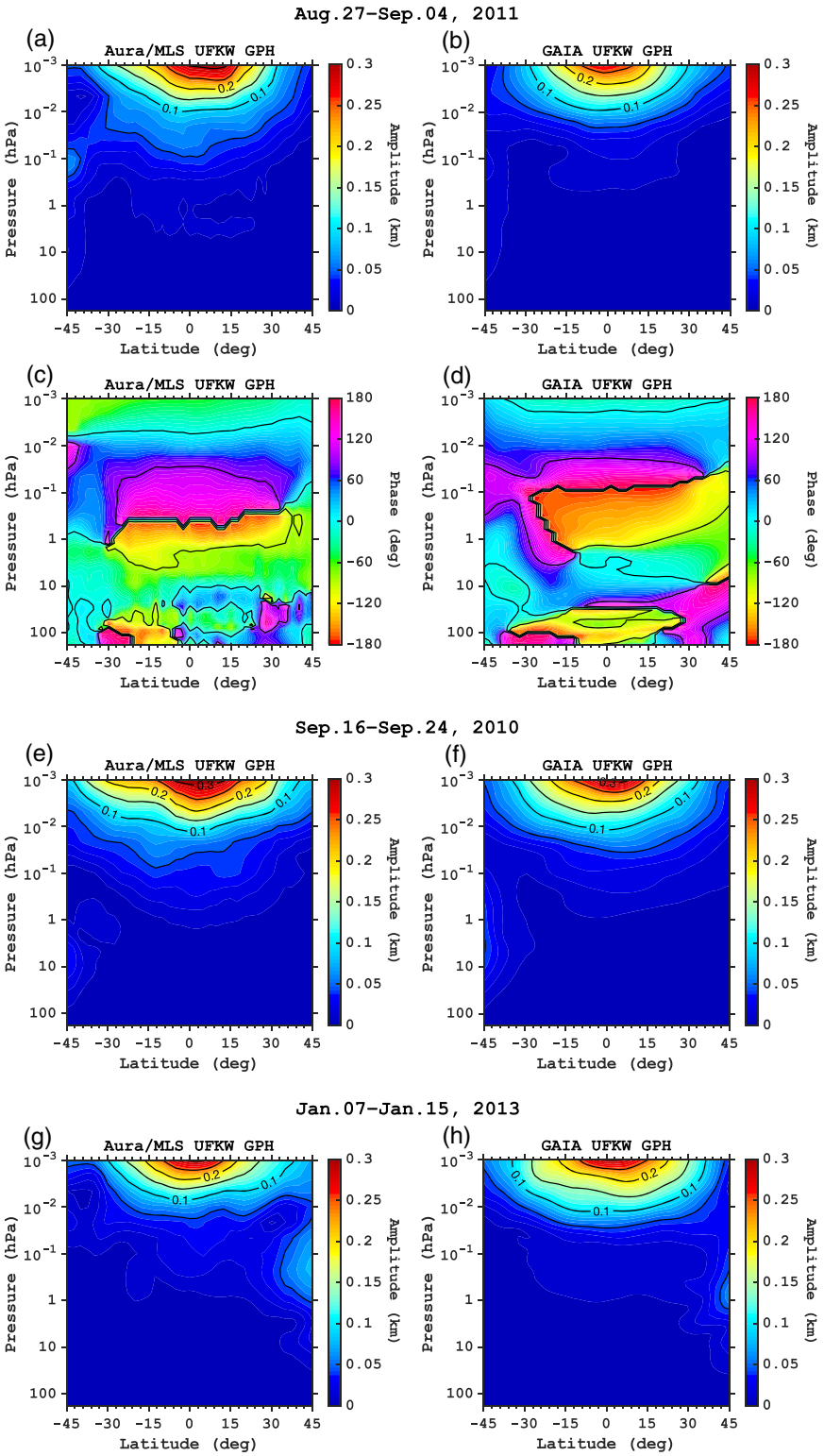

Figure 5. Latitude versus height structures of the ultrafast Kelvin wave (UFKW) in the geopotential height (GPH) during the August–September 2011 event (a–d), the September 2010 event (e, f), and the December 2012 to January 2013 event (g, h). The left panels are from the Aura Microwave Limb Sounder (MLS) measurements while the right panels are from the GAIA model. Panels (a, b, and e–h) show the amplitude while panels (c, d) show the phase.The vertical range covers the pressure levels from 261 to 0.001 hPa, which corresponds to approximately 9- to 97-km altitude.

January 2013, in which GAIA shows the largest wave activity. The model-data comparisons of the UFKW phase for the September 2010 event and the December 2012 to January 2013 event are presented in the supporting information, Figure S1.

3.2. UFKWs in the Thermosphere

Since the GAIA model is shown to be able to reproduce UFKW activity in the MLT region, which is well above the region constrained by meteorological reanalysis data (0–30 km), we now use GAIA to investigate the UFKW activity for the entire atmosphere. Figure 6 shows the amplitude and phase of the UFKW in the zonal wind (a, b), meridional wind (c, d), and temperature (e, f) for the August–September 2011 event. UFKW amplitudes in the zonal wind greater than 10 m/s are mainly confined within a latitude range of ±30° and an altitude range of 85–150 km. The peak amplitude of 35 m/s is found at 103-km altitude near the equator. Amplitudes in the meridional wind are relatively small, with the maximum value less than 10 m/s. The amplitude in the temperature reaches its maximum value of 14 K at 111-km altitude near the equator. Compared with the zonal wind amplitude, the temperature amplitude decays slowly with height above the amplitude peak. Gu et al. (2014) reported an amplitude of ~30 m/s in the zonal wind at 90- to 100-km altitude and 15 K in the temperature at 100- to 104-km altitude for the same event based on TIMED satellite measurements, which is in agreement with the GAIA results.

In the low-latitude MLT region, UFKW phases in the zonal wind and temperature tend to be horizontally uniform, and they show a downward phase propagation, which is consistent with the upward energy propagation. The vertical wavelength is ~40 km for the altitude range of 60–110 km for both the zonal wind and the temperature, which is in agreement with earlier observations (e.g., Davis et al., 2012). In the upper thermosphere, above 200 km or so, the phases are largely independent of height. The UFKW phase in the meridional wind shows a complex pattern in the low and middle atmosphere due to the small amplitude. In the upper thermosphere, the meridional wind phase is antisymmetric about the equator.

The vertical and horizontal structures of the UFKW in the zonal wind, meridional wind, and temperature presented in Figures 6a–6f are in good agreement with those by Chang et al. (2010) for an idealized TIME-GCM simulation. Similar results are obtained for the September 2010 event and the December 2012 to January 2013 event. The UFKW amplitudes in the zonal wind are presented in Figures 6g and 6h for these events. In both cases, the maximum amplitude in the zonal wind exceeds 30 m/s in the MLT region at the equator. Given that the GAIA model tends to underestimate the amplitude in the GPH in the MLT region (Figures 2–4), the actual zonal wind amplitude could be larger. In Figures S2 and S3, we plot the amplitudes and phases of the UFKW in the zonal wind, meridional wind, and temperature for the September 2010 event and the December 2012 to January 2013 event.

3.3. Ionospheric Variability During UFKW Events

We now turn our attention to the response of the ionosphere to the UFKW. GAIA's capability to reproduce the ionospheric response is verified through comparisons between observed and simulated UFKWs in the ionosphere. Ionospheric variability associated with the UFKW may be extracted from parameters such as TEC and EEF using formula (1). However, unlike the neutral atmosphere, the response of the ionosphere to the UFKW is highly dependent on local solar time (e.g., Chang et al., 2010; Gu et al., 2014). Therefore, fitting of (1) to observational and model data is performed at a fixed local solar time. In the following, we present the spectral component corresponding to the UFKW ($s = -1$, $\tau \sim 3$) in the ionosphere, as derived from the GOCE TEC observations and GAIA simulations, during the August–September 2011 event and the December 2012 to January 2013 event. Unfortunately, there is a large gap in the GOCE data during the September 2010 event, and thus, our analysis is limited to the other two events.

Figure 7 compares the UFKW spectral component in TEC observed by the GOCE satellite and simulated by the GAIA model during the August–September 2011 event. It is noted that in Figure 7, different color scales are adopted for different panels. The top panels (Figures 7a and 7b) present the background TEC at 7 p.m. local solar time, which corresponds to the ascending node of the GOCE orbit. These TEC values are calculated as the zonal and temporal mean within a 9-day moving window, which is also the time window used for calculating the amplitudes of the UFKW spectral component in Figures 7c–7f. In both the GOCE and GAIA results, the background TEC has a local maximum on both sides of the magnetic equator, reflecting the equatorial ionization anomaly (EIA) structure that is usually formed during the daytime due to the

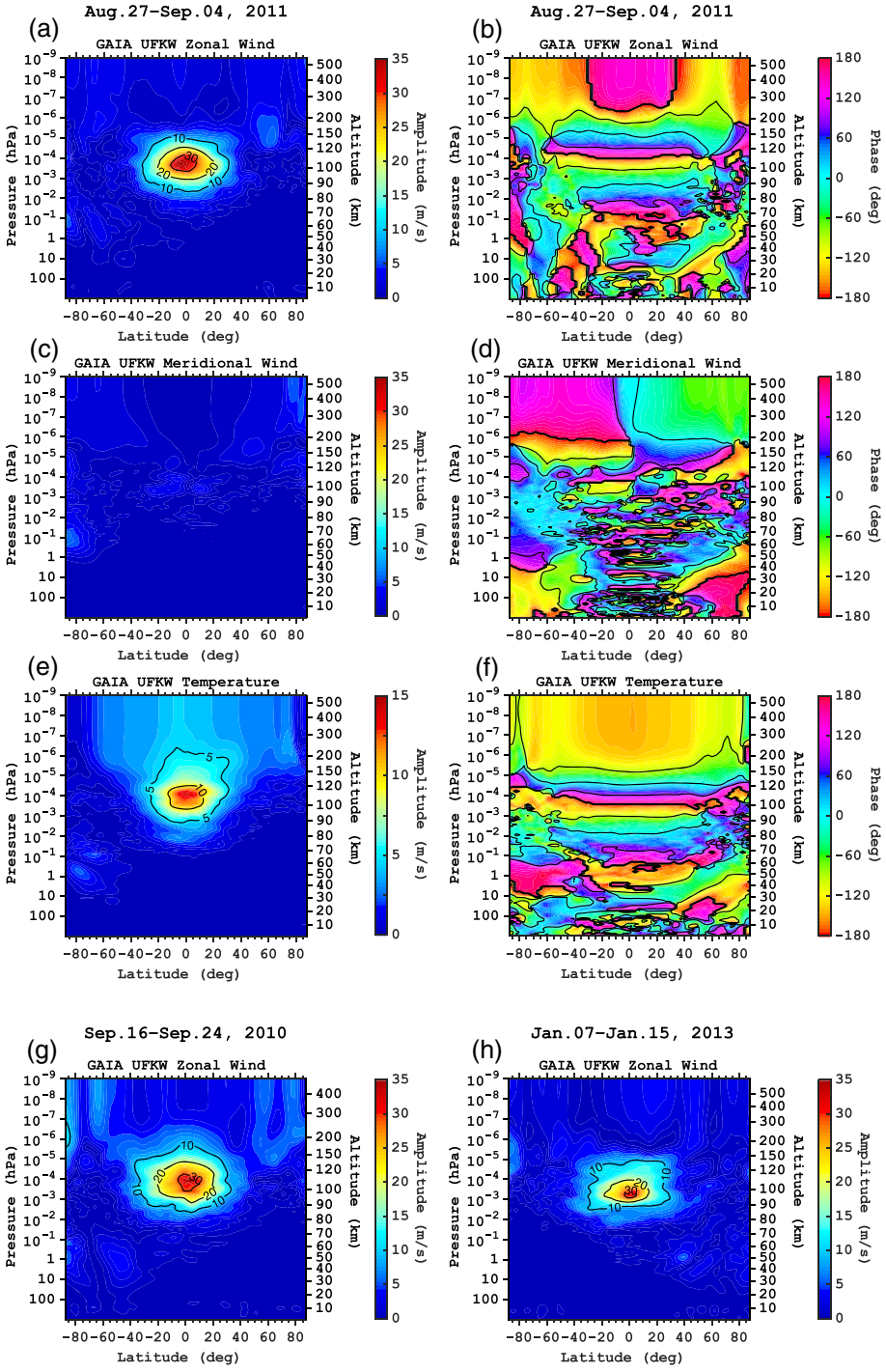

Figure 6. Latitude versus height structures of the ultrafast Kelvin wave (UFKW) in the zonal wind (a, b, g, h), meridional wind (c, d), and temperature (e, f) derived from the GAIA model. Panels (a–f) are for the UFKW event of August–September 2011 event, showing the amplitude on the left and the phase on the right. Panels (g) and (h) show the UFKW amplitude in the zonal wind during the September 2010 event and the December 2012 to January 2013 event, respectively. The UFKW is defined as the eastward-propagating wave with a period of 3.0 days and zonal wavenumber 1 for the August–September 2011 event and the December 2012 to January 2013 event, while for the September 2010 event, the wave with a period of 2.5 days is considered.

equatorial plasma fountain effect. The background TEC in GAIA is somewhat higher than that in GOCE observations, and also, the EIA crests are located at higher latitudes in GAIA than those derived from GOCE data. This could be due to an overestimation of the daytime EEF in GAIA, in other words, an

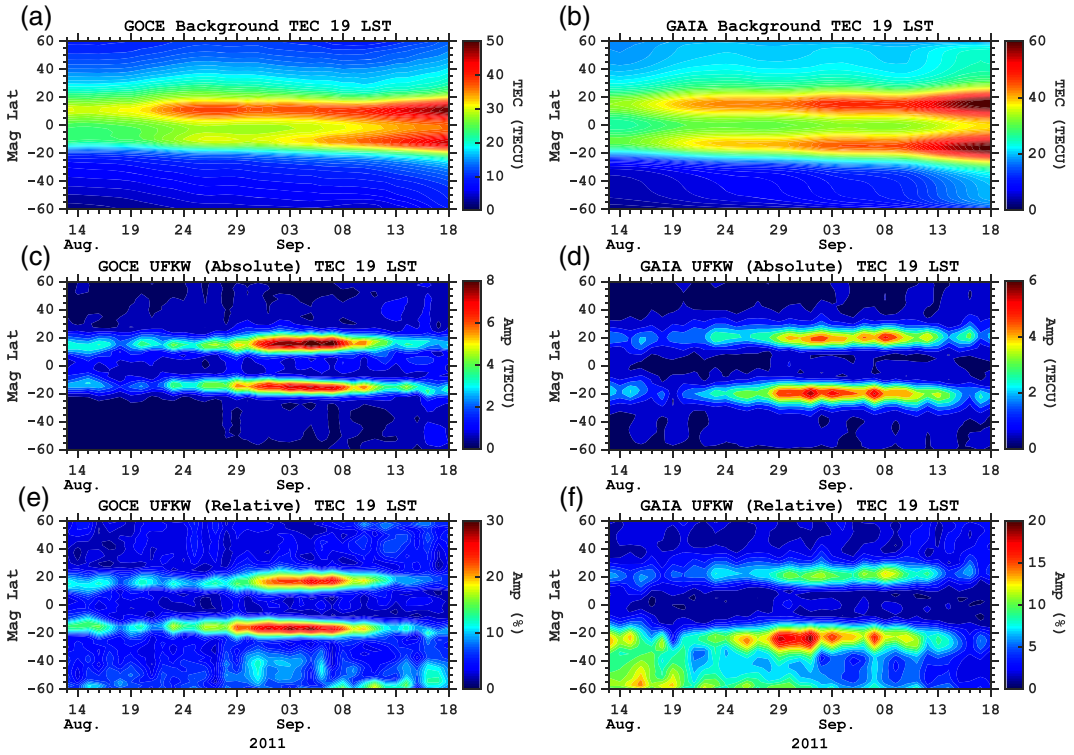

Figure 7. Comparison of the total electron content (TEC) at 7 p.m. local solar time derived from the GOCE measurements (a, c, e) and GAIA model (b, d, f). Panels (a, b) show the background TEC as defined here as the temporal and zonal mean calculated at each latitude using a 9-day moving window. Panels (c, d) show the amplitude of the ultrafast Kelvin wave (UFKW) spectral component in TEC calculated at each latitude using the 9-day moving window. The UFKW spectral component is defined as the largest amplitude of the eastward-propagating waves with zonal wavenumber 1 within periods 2.25–3.75 days. Panels (e, f) show the relative amplitude of the UFKW spectral component in TEC with respect to the corresponding background TEC value. Note that color scales are different for different panels.

overestimation of the equatorial plasma fountain effect. It is seen in Figures 7c and 7d that the amplitude of the UFKW spectral component in TEC also exhibits a double-peak structure. Local maxima of the amplitude occur at poleward edges of the EIA crests. The maximum amplitudes are ~8 TECU in the GOCE data and ~6 TECU in the GAIA model, which correspond to ~30% and ~20% of the background TEC, respectively (see Figures 7e and 7f).

Figure 8 presents model-data comparisons for the December 2012 to January 2013 event. The maximum amplitudes are, again, ~8 TECU (~30%) in the GOCE data and ~6 TECU (~20%) in the GAIA model, occurring at poleward edges of the EIA crests. The GOCE observations suggest that the ionospheric response is strongest around 5–10 February 2013, while in GAIA, the ionospheric response is more pronounced from end of December 2012 towards early January. This discrepancy can be attributed to the underestimation of UFKW forcing during early February 2013 (see Figure 4).

It is noted that there was an SSW event in January 2013 (Goncharenko et al., 2013). The central date of the SSW was on 7 January (Siddiqui et al., 2018), and associated ionospheric perturbations have been observed in the following days (Goncharenko et al., 2013; Jonah et al., 2014). This coincides with the period of enhanced UFKW activity in the middle atmosphere (Figure 4) and ionosphere (Figure 9). However, it is unclear if the UFKW event in January 2013 is related to the SSW, as UFKW bursts are also observed before and after the SSW. The relationship between SSW and UFKW is still under debate (e.g., England et al., 2012; Liu et al., 2012; Phanikumar et al., 2014; Sassi et al., 2013).

Figure 9 is the same as Figure 7 but for 7 a.m. local solar time, which corresponds to the descending node of the GOCE orbit. The GOCE TEC data reveal an enhancement in the amplitude of the UFKW spectral component at 0–20° magnetic latitudes during 30 August to 7 September 2011. This coincides with the time of enhanced UFKW activity observed in the ascending node. The absolute amplitude is small (~1.5 TECU at

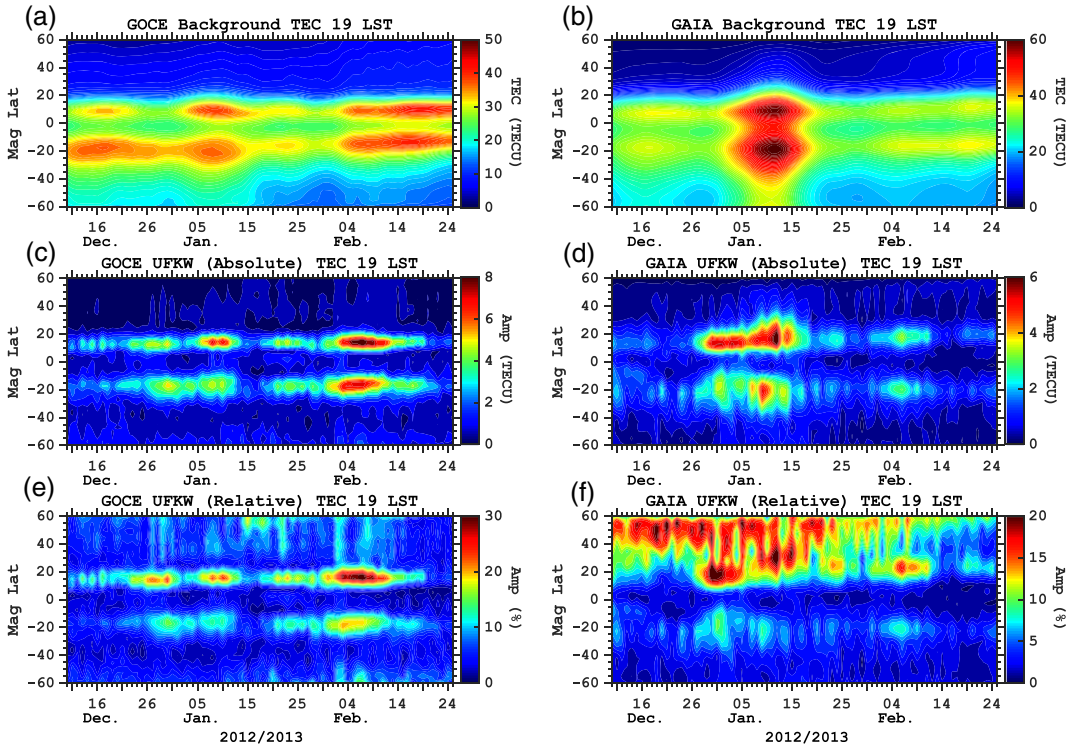

Figure 8. Same as Figure 7 except for the December 2012 to January 2013 event.

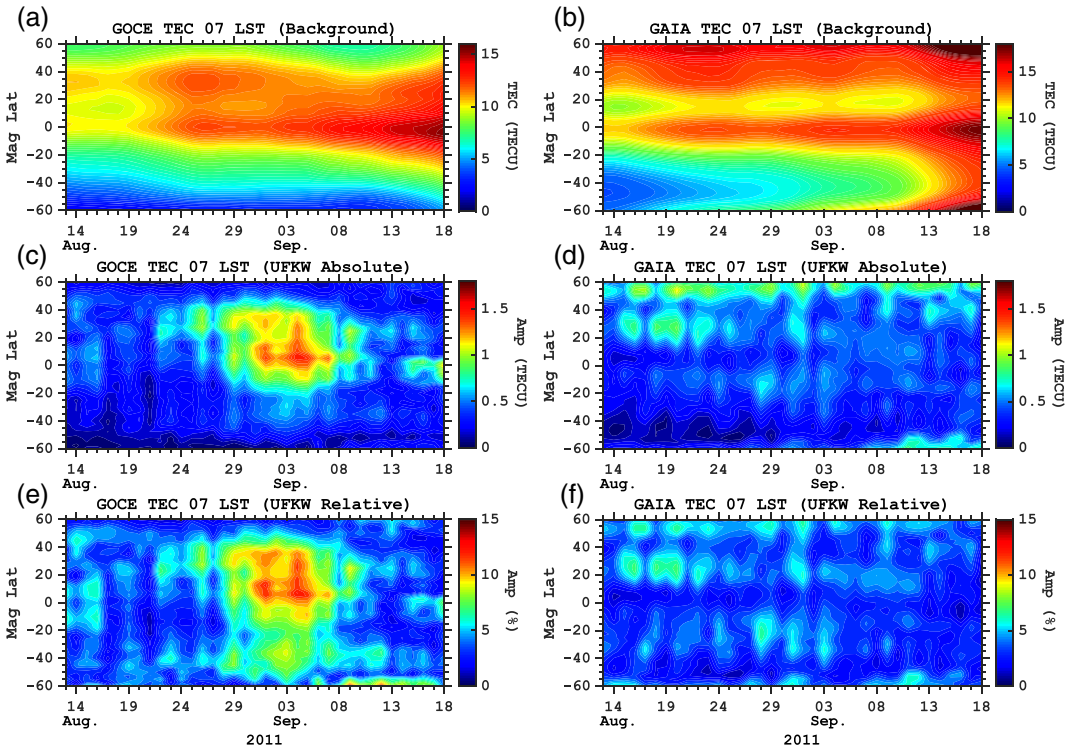

Figure 9. Same as Figure 7 except for 7 a.m. local solar time.

maximum), but the relative amplitude exceeds 10% of the background TEC. The GAIA does not reproduce the ionospheric response at this local solar time, possibly because of the underestimation of UFKW forcing in the model. Similarly, enhanced UFKW activity (~1.5 TEC, ~10%) was observed in the descending node during 29 January to 10 February 2013, and the GAIA model did not reproduce the observation (Figure S4).

Gu et al. (2014) analyzed global TEC maps derived from ground GPS data and investigated UFKW signatures during 2011. They showed the dependence of UFKW signatures in TEC on local solar time and magnetic latitude around the time of the August–September 2011 event, which gives us the opportunity to further validate the GAIA results. We show in Figures 10a and 10c the local solar time and magnetic latitude dependence of the background TEC and the amplitude of the UFKW spectral component in TEC during 27 August to 4 September 2011. Therein, the TEC values are evaluated at the ground level, not at 250-km altitude as in Figures 7–9. Our results are in good agreement with those presented by Gu et al. (2014) (see their Figures 5c and 5d).

Gu et al. (2014) also presented the dependence of the UFKW amplitude in the electron density (N_e) on magnetic latitude and on altitude using COSMIC data during 8–22 February 2011. In Figures 10b and 10d, we show similar results but for the August–September 2011 event. Despite the difference in the time intervals examined, our results agree qualitatively with those by Gu et al. (2014) (see their Figures 6a and 6b). In both results, the UFKW amplitude in N_e show local maxima at the poleward and equatorward edges of the EIA crests. This can be understood as a consequence of the equatorial plasma fountain effect. That is, when an eastward dynamo electric field is imposed on the dayside ionosphere, not only does the electron density at the EIA crests increase but the location of the EIA crests also moves poleward (Stolle et al., 2008). Thus, as the zonal electric field oscillates due to the UFKW, largest perturbations in the electron density tend to occur where the density gradient is most significant, which is not at the EIA crests but at their poleward and equatorward edges.

Figures 11a and 11b compare the spectra for the observed and simulated TEC at 7 p.m. local solar time at 250-km altitude near the northern EIA crest during the August–September 2011 event. In both cases, a spectral peak is visible at $s = -1$ and a period of ~3 days. A similar peak is found in the spectra for the daytime EEF at 110 km (Figure 11c) and for the equatorial zonal wind at the same height (Figure 11d). These results suggest that the EEF is modulated by the zonal wind, and subsequently, the plasma distribution in the EIA region is modulated by the EEF. As demonstrated by Yamazaki et al. (2014), the zonal wind at 100- to 120-km altitude in the equatorial region is effective in perturbing the dayside zonal electric field. The UFKW amplitude in the zonal wind happens to be largest in that region (Figure 6), allowing the UFKW to efficiently drive ionospheric variability. In Figure 11c, the spectra for the EEF are computed using only the daytime data between 7 a.m. and 5 p.m. local solar time. This is because the response of the EEF to the zonal wind is different during daytime and nighttime (Jin et al., 2008). Indeed, spectral patterns are different for daytime and nighttime EEFs, although zonal wind spectra are consistent between daytime and nighttime. This is demonstrated in Figure S5.

4. Discussion

In the previous section, we have validated GAIA's ability to reproduce ionospheric variability during UFKW events. In this section, we will investigate the simulated UFKW signatures in the ionosphere during the August–September 2011 event in more detail. We first discuss potential aliasing from other waves and tides into the UFKW spectrum component (i.e., $s = -1$ and τ~3 days) in the ionosphere. We then discuss the nature of the ionospheric variability during the UFKW event and possible detection of UFKW signatures using ground-based measurements. To facilitate the discussion, we have performed two numerical experiments as summarized in Table 1. In these numerical experiments, the neutral component of GAIA is decoupled from the ionospheric and electrodynamics models. The atmospheric temperature, winds, and composition are analyzed using the Fourier transform and reconstructed with the wave components having zonal wavenumbers from $s = -5$ to $s = +5$ only. In the first experiment "LARGE_WAVES," the ionospheric and electrodynamic models are forced with the reconstructed neutral fields. The main difference between the original GAIA simulation and LARGE_WAVES is that GAIA includes the waves that have relatively small spatial scales ($s > +5$ and $s < -5$), which are excluded in LARGE_WAVES. Also, GAIA takes into account the feedback process from the ionosphere to the neutral atmosphere, which is ignored in LARGE_WAVES. The

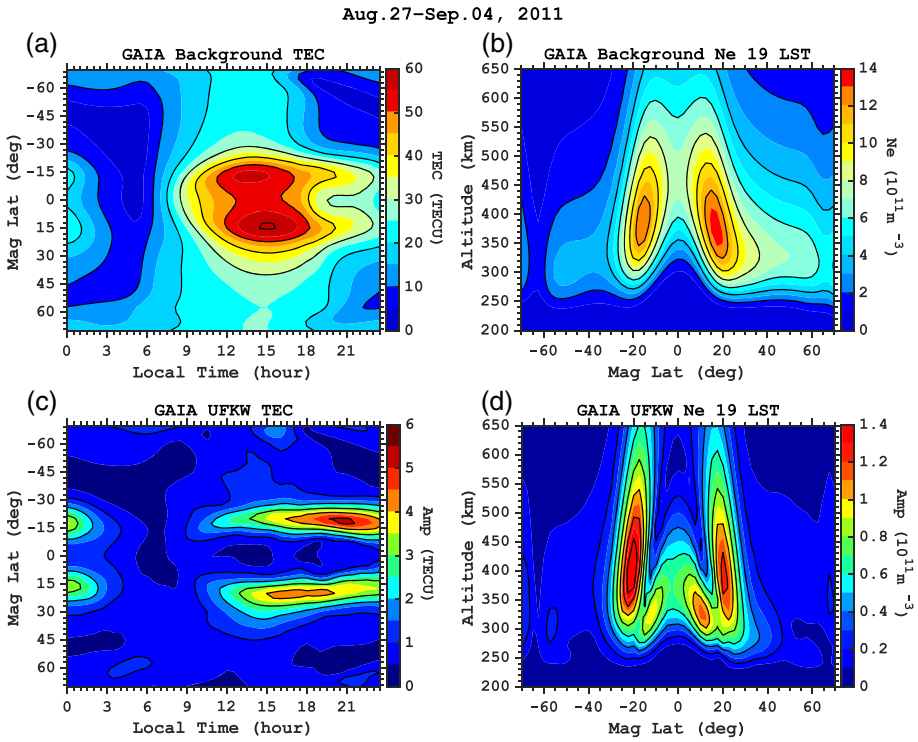

Figure 10. Spatial structure of the amplitude of the ultrafast Kelvin wave (UFKW) spectral component in total electron content (TEC) and electron density (N_e) during the August–September 2011 event. (a) Local time and magnetic latitude dependence of the background TEC. (b) Magnetic latitude and height dependence of the background electron density at 7 p.m. local solar time. (c) Same as (a) except for the the amplitude of the UFKW spectral component in TEC. (d) Same as (b) except for the amplitude of the UFKW spectral component in the electron density.

second experiment "NO_UFKW" is the same as LARGE_WAVES, but the E1 waves at periods 1.5–4.5 days are removed using the method of Hayashi (1971). This eliminates the UFKW in the neutral atmosphere and its direct influence on the ionosphere.

4.1. Aliasing

In section 3.3, the ionospheric variability associated with the UFKW was evaluated by fitting formula (1) to GOCE and GAIA TEC at a fixed local solar time. These fits can suffer from aliasing with various combinations of zonal wavenumber s and period τ. Here we discuss and identify potential sources of aliasing, and later, we will make an attempt to separate the aliasing sources from UFKW signatures in the ionosphere based on the controlled simulations, LARGE_WAVES and NO_UFKW.

Using the local solar time $t_{LT}\left(=t,+\frac{\lambda}{\Omega}\right)$, a wave $\cos\left(\frac{\Omega}{\tau}t+s\lambda\right)$ can be expressed as

$$\cos\left[\left(s-\frac{1}{\tau}\right)\lambda+\frac{\Omega}{\tau}t_{LT}\right]. \tag{2}$$

At a fixed local solar time, $\frac{\Omega}{\tau}t_{LT}$ is a constant, and thus, (2) is a function of longitude. In principle, the waves that have the same longitudinal dependence are indistinguishable. For the UFKW, $s=s_u\ (=-1)$ and $\tau=\tau_u\ (=\sim 3)$, and one cannot distinguish the UFKW from other waves that satisfy

$$\left|s-\frac{1}{\tau}\right|=s_u-\frac{1}{\tau_u}. \tag{3}$$

For global-scale waves, zonal wavenumber s needs to be an integer and period τ needs to be positive. Under these restrictions, there is a series of combinations (s, τ) that satisfy (3). Table 2 lists combinations (s, τ) for

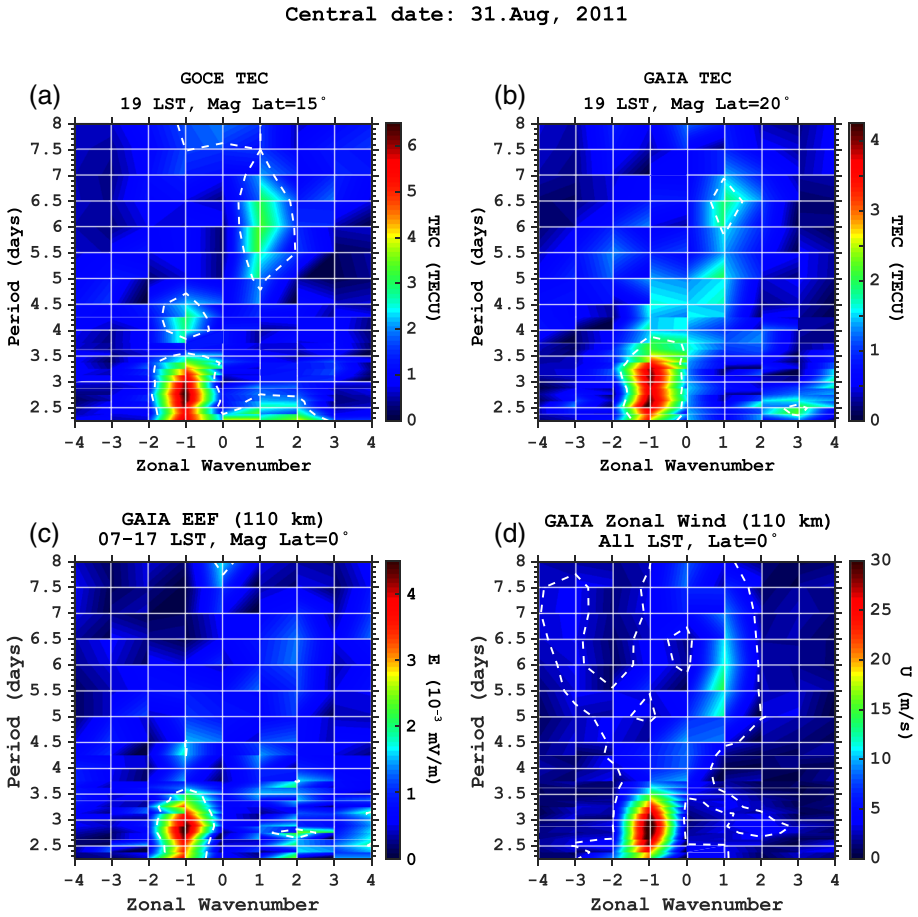

Figure 11. Wavenumber versus period spectra during the ultrafast Kelvin wave event of August–September 2011. Panel (a) is for the total electron content (TEC) derived from the GOCE measurements at 7 p.m. local solar time and 15° magnetic latitude. Panel (b) shows the same as (a) except for TEC at 20° magnetic latitude from the GAIA model. Panel (c) is also from GAIA but for the equatorial zonal electric field (EEF) between 7 a.m. and 5 p.m. local solar time at 110-km altitude. Panel (d) is for the zonal wind at the equator at 110-km altitude. The white dashed lines correspond to the 95% confidence level.

the waves from which aliasing can occur into the UFKW spectral component ($s_u = -1$, $\tau_u =$ 2–4 days) at a fixed local solar time. As it turns out, τ is negative if $s < 0$, so that aliasing does not occur from eastward-propagating waves. For $s \geq 0$, τ is mostly less than 1 day. The only wave with $\tau \geq 1.0$ day is $s = +2$ and $\tau = 1.33$–2.00 days. The mixed Rossby gravity wave, also known as the quasi 2-day wave, is westward-propagating with $s = +2$, $s = +3$, or $s = +4$ (e.g., Gu, Dou, et al. 2018), and thus, the $s = +2$ component is a potential source of aliasing. In general, quasi 2-day waves are strongest in the summer hemisphere. The $s = +2$ component in the MLT region attains its maximum amplitude in early August in the Northern Hemisphere and in mid-November in the Southern Hemisphere (Pancheva et al., 2018).

None of the waves in Table 2 has an overlap with tidal periodicities ($\tau = 1, \frac{1}{2}, \frac{1}{3}, \frac{1}{4}$ day); thus, aliasing from tidal waves does not occur as long as their amplitudes and phases stay constant. However, tides in the MLT region are known to be highly variable, and their amplitudes and phases can change significantly from one

Table 1
The Numerical Experiments Performed in This Study and the Wave Forcing Used Therein

Experiment	Waves
LARGE_WAVES	E5–W5, all periods
NO_UFKW	Same as LARGE_WAVES but excludes E1 with period 1.5–4.5 days

Table 2
Zonal Wavenumber s and Period τ (Days) of the Global-Scale Waves From Which Aliasing Into the Ultrafast Kelvin Wave (s = −1, τ = 2–4 Days) Spectral Component Can Occur When the Wave Signatures are Sampled at a Fixed Local Solar Time

s	τ	γ_{3h}	γ_{6h}	γ_{12h}	Possible sources
0	0.67–0.80	0.97	0.90	0.64	UFKW × S1
+1	0.40–0.44	0.90	0.64	0.00	UFKW × S2
+2	1.33–2.00	0.97	0.90	0.64	Q2DW, UFKW × S1
+2	0.29–0.31	0.78	0.30	0.21	UFKW × S3
+3	0.57–0.67	0.90	0.64	0.00	UFKW × S2
+3	0.22–0.24	0.64	0.00	0.00	UFKW × S4
+4	0.36–0.40	0.78	0.30	0.21	UFKW × S3
+4	0.18–0.19	0.47	0.18	0.13	UFKW × S5

Note. Aliasing effects are reduced when the wave signatures are sampled over a range of local solar time (e.g., 3, 6, and 12 h), which is expressed in terms of the amplitude ratio γ with respect to the amplitude calculated by sampling wave signatures at a single local time. Possible sources of aliasing are also indicated, where the × represents the nonlinear interaction between the ultrafast Kelvin wave (UFKW) and migrating tides, with S1, S2, S3, S4, and S5 signifying $n = 1$ (diurnal tide), $n = 2$ (semidiurnal tide), $n = 3$ (terdiurnal tide), $n = 4$, and $n = 5$, respectively, and the Q2DW standing for the quasi 2-day wave.

day to the next (e.g., Fang et al., 2013; Miyoshi & Fujiwara, 2003). Short-term tidal variability will inevitably contribute to the spectral components listed in Table 2. One of the causes of day-to-day tidal variability is the nonlinear interaction between tides and other waves, which generate secondary waves at periods close to tidal periodicities and hence modulate the tides (e.g., Chang et al., 2011; Pedatella et al., 2012). In the following, we consider aliasing by the waves generated through the nonlinear interaction of the UFKW and tides.

According to the theory of Teitelbaum and Vial (1991), the nonlinear interaction of two global-scale waves can give rise to secondary waves with frequencies and zonal wavenumbers that are the sums and differences of those of the interacting waves. Thus, the nonlinear interaction between an UFKW $\cos\left(\frac{\Omega}{\tau_u}t + s_u\right)$ and tidal wave $\cos(n\Omega t + s\lambda)$ leads to secondary waves:

$$\cos\left[\left(\frac{\Omega}{\tau_u} \pm n\Omega\right)t + (s_u \pm s)\lambda\right], \tag{4}$$

where $n = 1, 2, 3$ represent oscillations with periods corresponding to 1 (diurnal tide), $\frac{1}{2}$ (semidiurnal tide), and $\frac{1}{3}$ day (terdiurnal tide), respectively. In the local time frame, this becomes

$$\cos\left[\left(s_u \pm s - \frac{1}{\tau_u} \mp n\right)\lambda + \left(\frac{\Omega}{\tau_u} \pm n\Omega\right)t_{LT}\right], \tag{5}$$

Therefore, at a fixed local solar time, aliasing into the UFKW (s_u, τ_u) occurs if

$$\left|s_u \pm s - \frac{1}{\tau_u} \mp n\right| = s_u - \frac{1}{\tau_u}. \tag{6}$$

Since s and n are required to be an integer and a natural number, respectively, the only possible solution is

$$n = s, \tag{7}$$

that is, migrating tides. In other words, secondary waves generated by the nonlinear interaction of the UFKW and migrating tides cannot be distinguished from the UFKW when the wave signatures are sampled at a fixed local solar time. For example, the nonlinear interaction between the UFKW ($s = -1$, $\tau = 3$ days) and migrating diurnal tide ($s = +1$, $\tau = 1$ day) leads to secondary waves with ($s = 0$, $\tau = 0.75$ day) and ($s = +2$, $\tau = 1.5$ day), both of which can be found in Table 2. In fact, for each wave in Table 2, it is possible to find a pair of the UFKW and migrating tide that can be a potential source of aliasing.

Aliasing effects are expected to reduce when the wave signatures are sampled over a range of local solar time instead of a single local solar time. To confirm this, we generated synthetic data by sampling the waves listed in Table 2 over a range of local solar time (e.g., 9 a.m. to 3 p.m.). The amplitude of the UFKW spectral component ($s = -1$, $\tau = 3$ days) was calculated by fitting (1) to the synthetic data. The derived amplitude is compared with that calculated with the synthetic data sampled at a fixed local solar time (e.g., 12 noon). The amplitude ratio γ is listed in Table 2 for ranges of local solar time 3, 6, and 12 h. As expected, aliasing effects are smaller when the data from a wider range of local solar time are included in the wave analysis. For instance, aliasing from the wave ($s = +1$, $\tau = 0.40$–0.44d day) can be largely avoided, if the data are included for the whole daytime period, which corresponds to a local time range of 12 h.

The controlled simulations, LARGE_WAVES and NO_UFKW, help us understand aliasing effects in the UFKW spectral component that we presented in section 3.3. Figure 12a is the same as Figure 11d but

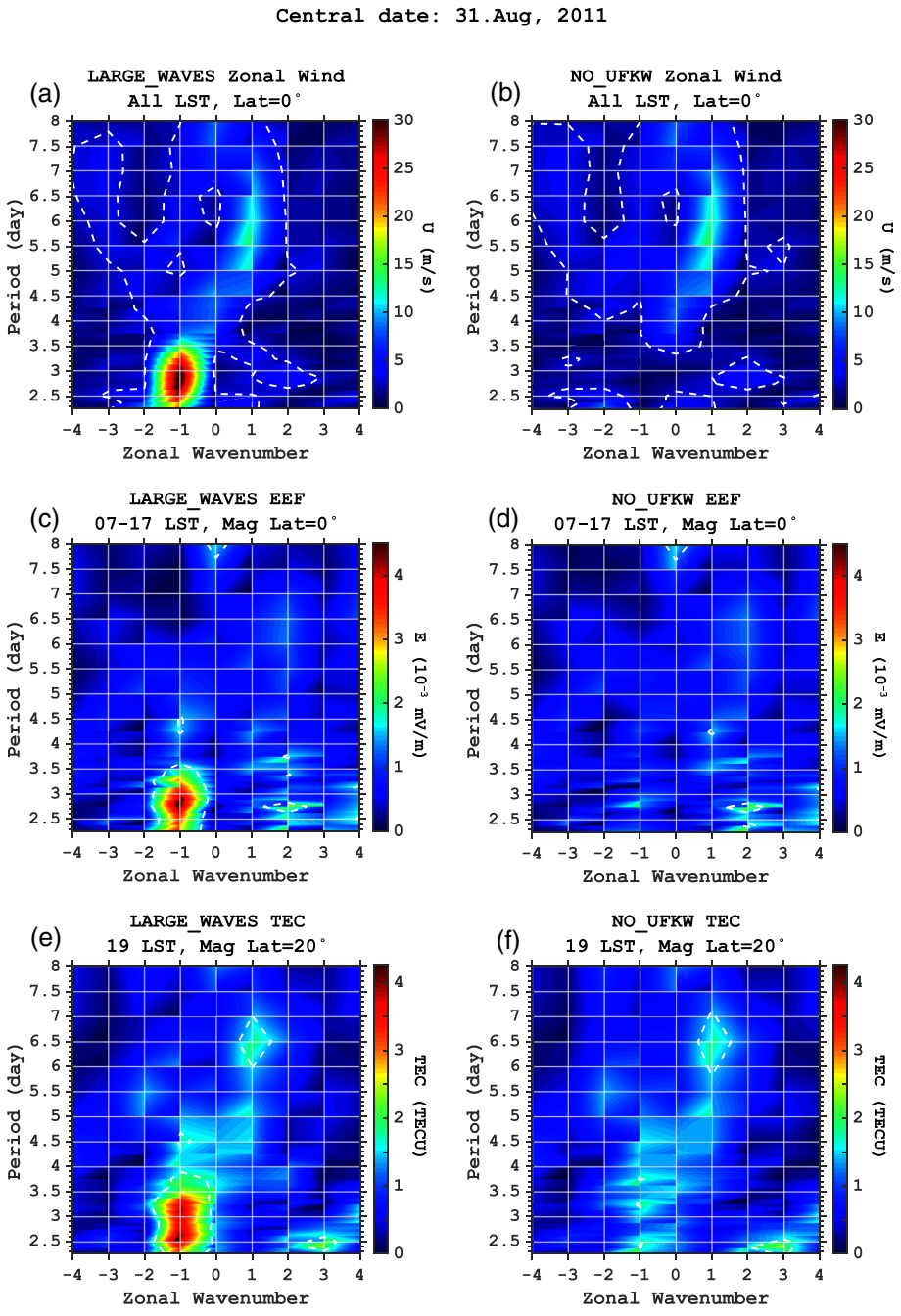

Figure 12. Wavenumber versus period spectra during the ultrafast Kelvin wave event of August–September 2011. Panels (a) and (b) are the same as Figure 11d except for LARGE_WAVES and NO_UFKW simulation cases, respectively. Panels (c) and (d) are the same as Figure 11c except for LARGE_WAVES and NO_UFKW simulation cases, respectively. Panels (e) and (f) are the same as Figure 11b except for LARGE_WAVES and NO_UFKW simulation cases, respectively.

derived from LARGE_WAVES, showing the zonal wavenumber spectrum of the equatorial zonal wind at 110 km during the August–September 2011 event. It is noted that the wave analysis includes the zonal wind data from all local solar times. The results from GAIA (Figure 11d) and LARGE_WAVES (Figure 12a) are almost identical, indicating that the feedback effect from the ionosphere to the neutral atmosphere, which is taken into account in GAIA but not in LARGE_WAVES, does not play a significant role for global-scale waves at 110 km. Figure 12b shows the spectrum derived from NO_UFKW, which

eliminates the E1 waves with periods ~3 days. The spectral pattern is consistent with that of LARGE_WAVES in Figure 12a except for the absence of the UFKW.

Figure 12c presents the zonal wavenumber spectrum of the EEF as derived from LARGE_WAVES. It is noted that only daytime data (7 a.m. to 5 p.m.) are included in the wave analysis. The result shows a spectral peak at $s = -1$ and $\tau \sim 3$ days, in good agreement with the GAIA simulation (Figure 11c). In the NO_UFKW run (Figure 12d), the spectral peak is reduced below the 95% confidence level. These results suggest that the spectral peak in the daytime EEF at $s = -1$ and $\tau \sim 3$ days during the August–September 2011 event is directly caused by the UFKW.

Figures 12e and 12f show zonal wavenumber spectra of TEC at 7 p.m. local solar time as derived from LARGE_WAVES and NO_UFKW, respectively. The LARGE_WAVES simulation case reveals enhanced wave activity at $s = -1$ and $\tau \sim 3$ days, which is consistent with the GAIA result (Figure 11b) as well as GOCE observation (Figure 11a). It is interesting to note that wave activity at $s = -1$ and $\tau \sim 3$ days is also seen in NO_UFKW, which excludes forcing by the UFKW. There are at least three significant peaks in the E1 spectrum at periods 2–4 days. Each peak has a spectral amplitude ~1.8 TEC, which is about half the amplitude of the UFKW spectral component in LARGE_WAVE (~4 TEC). These spectral peaks in NO_UFKW TEC are due to aliasing from westward-propagating waves with $\tau \leq 2.0$ days as listed in Table 2. These results suggest that UFKW activity in the ionosphere observed at a fixed local solar time is contributed not only by the UFKW but also by other waves, such as secondary waves due to the nonlinear interaction between the UFKW and migrating tides as discussed earlier.

4.2. Ground Observer Perspective

Up to now, we have mainly considered the ionospheric response to the UFKW from a perspective of the GOCE satellite at a fixed local solar time. We now discuss the wave effect from a ground observer perspective. For a ground observer at a fixed geographical location, the UFKW manifests as a ~3-day oscillation of atmospheric parameters. Therefore, the question is whether the ~3-day variation caused by the UFKW is substantially larger than ~3-day variations due to other causes.

Figure 13a depicts the temporal and longitudinal variations of the equatorial zonal wind at 110 km during 15 August to 20 September 2011 as derived from the LARGE_WAVES simulation. A 24-h average was applied to the wind data at each longitude in order to suppress the variations associated with tides with periods less than 1 day. The zonal wind shows large day-to-day variability about ±60 m/s. There is a hint of E1 wave activity with a period of ~3 days from end of August towards beginning of September. Figure 13d is the same as Figure 13a, but a bandpass filter is applied at each longitude to extract the variations with periods 1.5–4.5 days. Enhanced E1 wave activity is more clearly visible. Figure 13g presents the corresponding result from the NO_UFKW simulation, which does not include E1 waves with periods of 1.5–4.5 days. In this case, ~3-day variability can arise from ~3-day waves with other zonal wavenumbers (i.e., W5–W1, S0, E2–E5) as well as from secondary waves due to the nonlinear interaction between tides and ~3-day waves. In Figure 13g, ~3-day variability is much weaker than in Figure 13d, indicating that the UFKW is the leading cause of ~3-day variations for a ground observer at a fixed longitude. Similar results were obtained for equatorial zonal winds at lower altitudes in the MLT region (not shown here). Thus, it is possible to detect UFKW signatures using a ground-based instrument such as a meteor radar (e.g., Vincent, 1993).

The results are presented in a similar format for the EEF at 110 km in Figures 13b, 13e, 13h, and 13k and for TEC at 20° magnetic latitude in Figures 13c, 13f, 13i, and 13l. For these ionospheric parameters, the contributions of the UFKW (Figures 13h and 13i) and non-UFKW sources (Figures 13k and 13l) are comparable, and the relative contribution of the two depends on longitude. The ~3-day variations due to the UFKW and other sources could strengthen or cancel each other depending on their phases. Thus, a ground observer does not necessarily detect enhanced ~3-day ionospheric variability even during times of enhanced UFKW activity. The same conclusion was reached when the ionospheric parameters at a fixed local solar time were analyzed at each longitude. Figure S6 shows plots similar to those in Figure 13 but derived using the EEF at 12 noon local solar time and TEC at 7 p.m. local solar time.

It may be noted in Figures 13k and 13l that the amplitude of ~3-day ionospheric variations caused by the UFKW depends on longitude. This is, in part, due to the longitudinal variation of the geomagnetic field. The Earth's main magnetic field plays an important role for the ionospheric electrodynamics (Takeda,

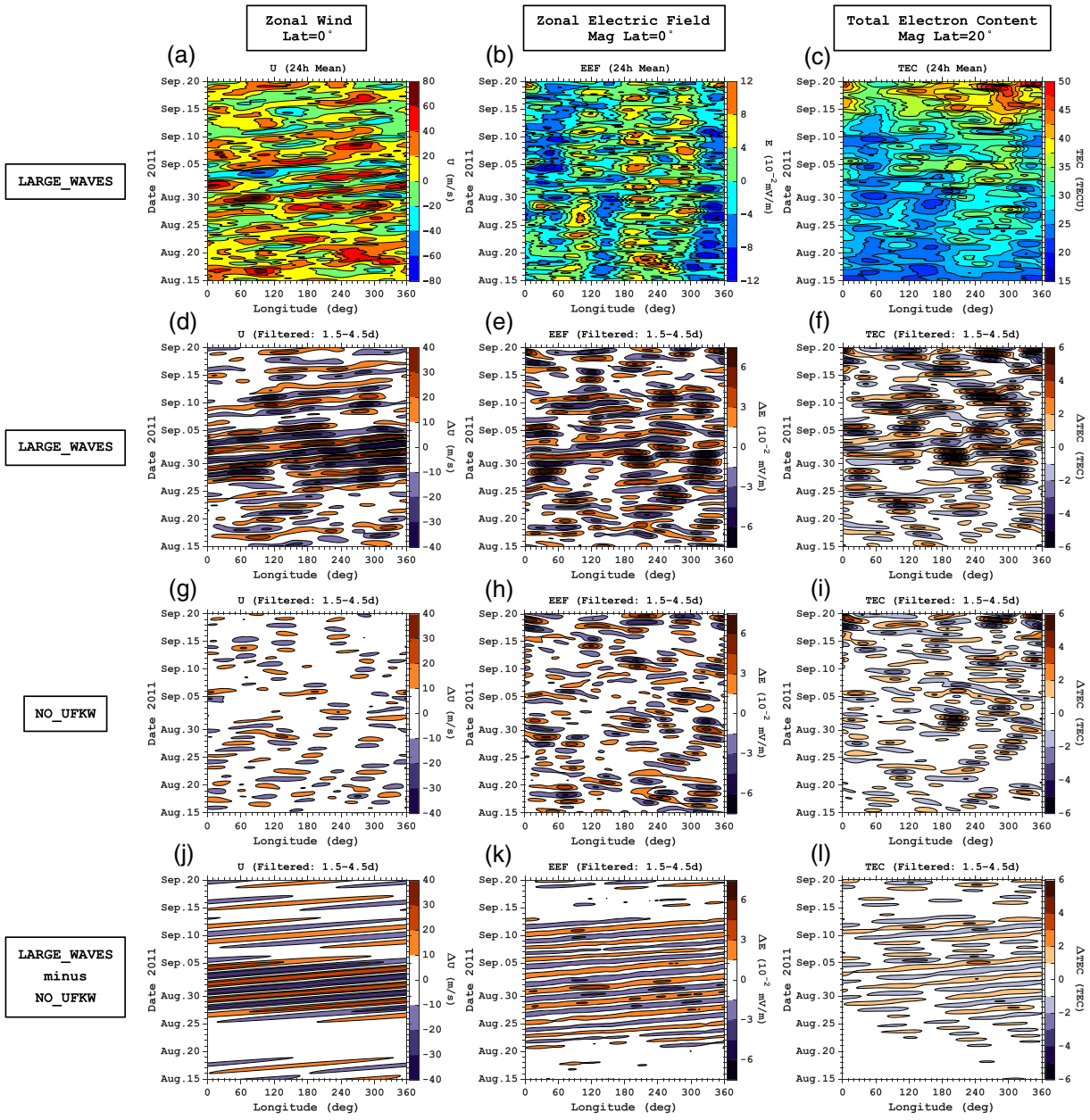

Figure 13. (a–c) Longitude versus time diagrams for the 24h mean of (a) the equatorial zonal wind at 110-km altitude, (b) equatorial zonal electric field (EEF) at 110-km altitude, and (c) total electron content (TEC) derived from the LARGE_WAVES simulation case. (d–e) The same as (a–c) but the 1.5- to 4.5-day bandpass filter is applied at each longitude to extract ~3-day variations. (g–i) The same as (d–e) except for the NO_UFKW simulation case. (j–l) The difference between LARGE_WAVES and NO_UFKW simulation cases, isolating the effect of the ultrafast Kelvin wave.

1996; Cnossen & Richmond, 2013) and its zonal structure can be imprinted in ionospheric parameters (Yue et al., 2013). Since the GAIA model assumes a simple dipole magnetic field that is tilted against the Earth rotation axis, the longitudinal asymmetry of ionospheric variations associated with the UFKW could be more pronounced in the real geomagnetic field configuration.

4.3. Ground-Based Magnetometer Detection of the UFKW

The results presented above suggest that during times of high UFKW activity, an enhancement occurs in the spectral component of the ionospheric variability corresponding to the UFKW (i.e., period $\tau \sim 3$ days and zonal wavenumber $s = -1$) (Figures 11 and 12), but this does not necessarily lead to an enhancement in

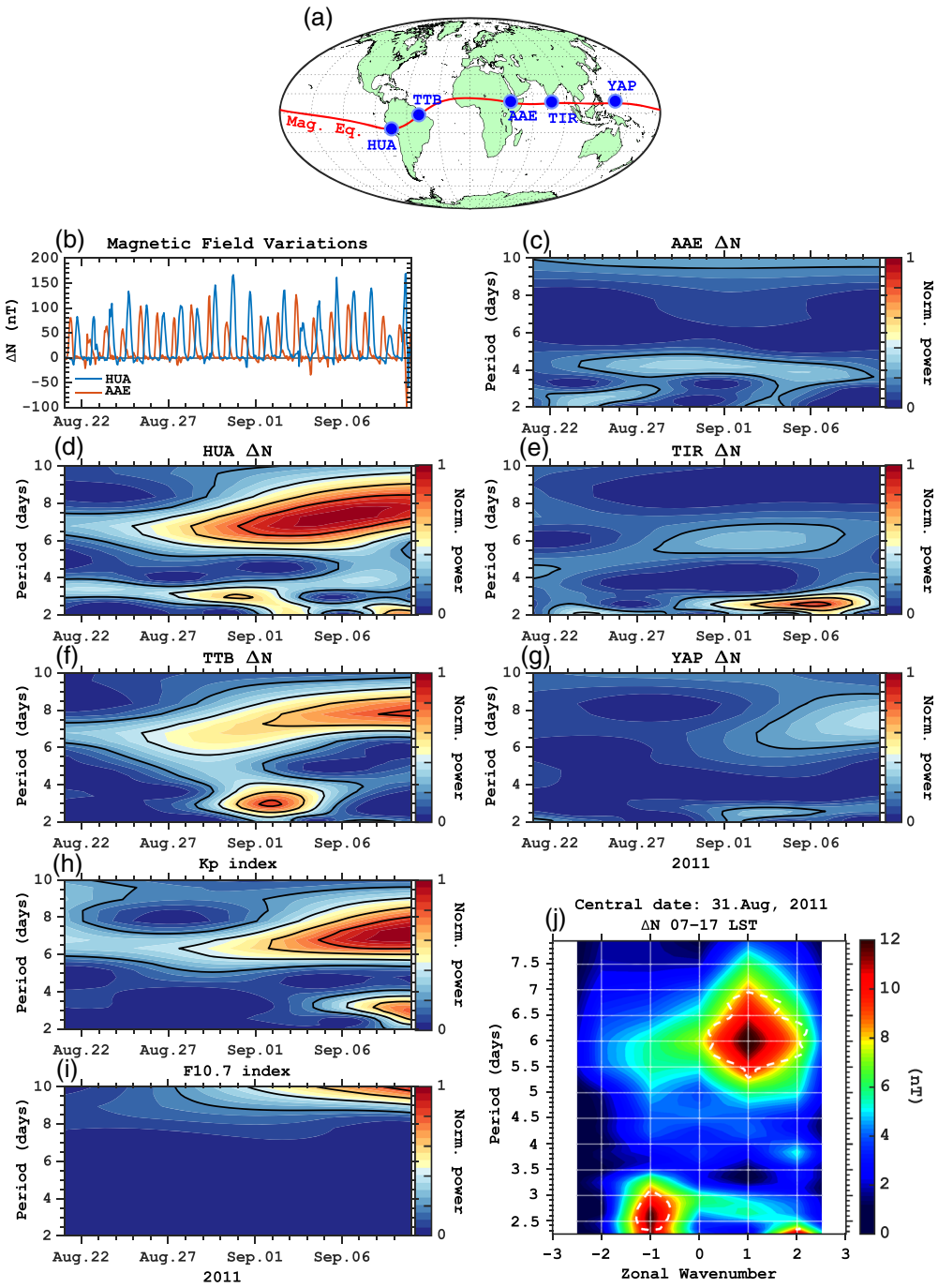

Figure 14. (a) Locations of the magnetic observatories: HUA = Huancayo; TTB = Tatuoca; AAE = Addis Ababa; TIR = Tirunelveli; and YAP = Yap Island. The red line denotes the magnetic equator. (b) Examples of magnetic field perturbations in the magnetic-northward component (ΔN) at Huancayo and Addis Ababa during 21 August to 9 September. (c–g) Wavelet spectra of ΔN at different observatories as a function of time and period. Spectral power is normalized to the maximum value at Huancayo. (h) Wavelet spectrum of the geomagnetic activity index *Kp*. Spectral power is normalized to the maximum value. (i) Wavelet spectrum of the solar activity index $F_{10.7}$. Spectral power is normalized to the maximum value. (j) Wavenumber versus period spectrum of ΔN derived from the combination of the daytime ΔN data from the five observatories. The white dashed lines correspond to the 95% confidence level.

~3-day ionospheric variations at a fixed longitude due to the presence of other ~3-day variability (Figure 13). Keeping this in mind, we examine ground-based magnetometer data during the UFKW event of August–September 2011 and discuss the possible detection of UFKW signatures.

Figure 14a shows the distribution of the ground-based magnetometers used in this study. As mentioned earlier, these five observatories are all located in the vicinity of the magnetic equator, and thus, the magnetic perturbations in the magnetic northward component (ΔN) are predominantly due to the equatorial electrojet, which is closely associated with the EEF. Examples of ΔN data are plotted in Figure 14b for Huancayo and Addis Ababa. In general, ΔN is very small at night because of the absence of the equatorial electrojet due to low ionospheric conductivities, and ΔN is usually positive during the day, reflecting the eastward current flow of the equatorial electrojet, with a daily maximum around 11 a.m. local solar time. The daily maximum values exhibit day-to-day variability, which is mostly due to day-to-day variations of the EEF (Yamazaki, Stolle, Matzka, Liu, et al. 2018).

Figures 14c–14g show wavelet power spectra of ΔN at different locations. The wavelet analysis is based on the technique detailed by Torrence and Compo (1998). A similar method has been used in previous studies to examine spectral features of the equatorial electrojet and discuss their possible connections with atmospheric waves (e.g., Gurubaran et al., 2011; Jarvis, 2006; Ramkumar et al., 2009). In our wavelet analysis, the data are included for both daytime and night time. The results are similar when the night time data are excluded. The wavelet spectrum of ΔN at Huancayo (Figure 14d) reveals the presence of relatively large ~3-day variations from end of August to beginning of September 2011. The spectrum at the closest observatory, Tatuoca (Figure 14f), shows a similar pattern but with maximum activity of ~3-day variations on 2 September slightly later than that at Huancayo on 31 August. Although the two observatories are less than 30° apart in longitude, the behavior of the equatorial electrojet could be different as discussed in detail by Soares, Yamazaki, Matzka, et al. (2018). In both Huancayo and Tatuoca results, there is a broader spectral peak at 5–10 days. This could be due to changes in geomagnetic activity, which is known to affect the equatorial electrojet (e.g., Xiong et al., 2016; Yamazaki & Kosch, 2015). In Figure 14h, the wavelet spectrum is presented for the geomagnetic activity index *Kp*. The spectral peak around 5–10 days is visible from end of August 2011 for the rest of the period. Another possible source of the 5- to 10-day variations is the quasi 6-day wave, which leads to a ~6-day modulation of the equatorial electrojet (Yamazaki, Stolle, Matzka & Alken, 2018).

The equatorial electrojet is also affected by solar activity (e.g., Matzka et al., 2017). We plot the wavelet spectrum of the solar activity index $F_{10.7}$ in Figure 14i. On the time scale of our interest, variations of $F_{10.7}$ are mainly at the period of the solar rotation and its harmonics (27, 13.5, and 9 days) and thus would make little contribution to ~3-day variations of the equatorial electrojet. The wavelet spectra of ΔN for Addis Ababa, Tirunelveli, and Yap Island are presented in Figures 14c, 14e, and 14g, respectively. They are only in partial agreement with one another and with those for Huancayo (Figure 14d) and Tatuoca (Figure 14f). For instance, at Addis Ababa (Figure 14c), ~3-day and 5- to 10-day variations, which are identified in the Huancayo and Tatuoca data, are barely visible in the wavelet spectrum. The lack of the 5- to 10-day variations could result from the longitudinal asymmetry in the response of the equatorial electrojet to geomagnetic activity (e.g., Maute et al., 2015) as well as to the quasi 6-day wave (Yamazaki, Stolle, Matzka & Alken 2018). At Tirunelveli (Figures 14e) and Yap Island (Figures 14g), variations at a period of 2–3 days are seen in wavelet spectra, but they occur a few days after those at Huancayo and Tatuoca. These discrepancies highlight the difficulty to confidently identify the UFKW activity from the magnetic data obtained at a single location.

Next, the zonal wavenumber spectrum is derived by fitting formula (1) to the daytime ΔN data at the five observatories. The zonal wavenumbers only from -2 to $+2$ are considered due to the limited longitudinal coverage of the stations (Figure 14a). The result presented in Figure 14j reveals a significant peak at periods 2.5–3 days with zonal wavenumber $s = -1$. This is consistent with the result for the daytime EEF derived from the GAIA model (Figure 11c). In Figure 14j, there is also a spectral peak at a period ~6 days with zonal wavenumber s from 0 to +2. This can be due to the superposition of the geomagnetic activity effect, which is mainly at $s = 0$ (Pancheva et al., 2008) and the effect of the quasi 6-day wave, which is mainly at $s = +1$ (Yamazaki, Stolle, Matzka & Alken 2018).

As we showed earlier using controlled simulations (Figures 12c and 12d), the spectral peak of the daytime equatorial electric field at a period of ~3 days with zonal wavenumber $s = -1$ is directly caused by the UFKW. We found a similar spectral peak in the equatorial electrojet derived with ground-based magnetometer data. This is the first time that magnetic signatures of the UFKW in the equatorial electrojet are

detected. It supports our hypothesis from the numerical experiments that UFKW activity leads to an enhancement of the spectral component in the ionosphere with period τ~3 days and zonal wavenumber $s=-1$, although ~3-day variations are not necessarily observed at a fixed longitude. This underlines the importance of multipoint measurements when UFKW signatures in the ionosphere are investigated using ground-based observations. A multipoint measurement approach was used in the past in attempts to observe ionospheric signatures associated with the quasi 2-day wave, quasi 6-day wave, and fast Kelvin wave from the ground (Pancheva et al., 2006, 2008). Our results support such an approach for studying the UFKW.

5. Summary and Conclusions

In this study, we use the whole atmosphere model GAIA to simulate equatorial Kelvin waves with a period of ~3 days, also known as UFKWs. We examine the UFKW events of September 2010, August–September 2011, and December 2012 to January 2013, which are particularly strong according to the 16 years of GPH measurements by the Aura MLS (Figure 1). As we constrain the lower layers of GAIA below 30 km with meteorological reanalysis data, the model is able to reproduce main characteristics of UFKWs in the MLT region as observed by the Aura/MLS (Figures 2–5). According to the GAIA results, the zonal wind amplitude exceeds 30 m/s in the lower thermosphere (95–110 km) during these events (Figure 6), which is consistent with the earlier observations by Gu et al. (2014) during the August–September 2011 event.

GAIA is also able to reproduce wave activity in the TEC retrieved from GPS observations by the GOCE satellite at ~7 p.m. local solar time (Figures 7 and 8). The GOCE data reveal the amplitude of the UFKW spectral component being up to 8 TECU (30% of the background) at ±15° magnetic latitudes, while the model data show the smaller amplitude up to 6 TECU (20% of the background) at ±20° magnetic latitudes. The GOCE data also show the wave activity at ~7 a.m. local solar time with the amplitude up to 1.5 TECU (10% of the background), which the GAIA model does not capture well (Figure 9). The dependence of the amplitude of the UFKW spectral component in TEC on magnetic latitude, local solar time, and altitude during the August–September 2011 event (Figure10) is consistent with the earlier report by Gu et al. (2014). The TEC response to the UFKW can be explained by the modulation of the EEF (and thus the equatorial plasma fountain) by the zonal wind (Figure 11), confirming the earlier finding by Chang et al. (2010).

Numerical experiments are performed for the August–September 2011 event to examine the nature of the ionospheric variability associated with the UFKW. When the UFKW is excluded from the neutral atmosphere, the amplitude of the UFKW spectral component ($s=-1$, τ~3) in the ionosphere is substantially reduced (Figure 12). This establishes that the UFKW causes eastward-propagating ~3-day ionospheric variations with zonal wavenumber 1. The UFKW spectral component in the ionosphere at a fixed local time is subject to aliasing from other waves, such as secondary waves due to the nonlinear interaction between the UFKW and migrating tides (Table 2), but the total contribution of those waves to the UFKW spectral component is less than the direct contribution by the UFKW.

Numerical results also suggest that it can be difficult for a ground observer to distinguish between ~3-day ionospheric variations associated with the UFKW and those caused by other sources, as they have comparable amplitudes even during times of enhanced UFKW activity (Figure 13). We highlight this issue using ground-based magnetometer measurements of the equatorial electrojet during the UFKW event of August–September 2011. The wavelet spectra of the magnetometer data at different observatories are only in partial agreement, with or without a spectral peak around 3 days. Despite that, the combination of the data reveals the predominance of the wave component with a period of ~3 days and zonal wavenumber $s=-1$, corresponding to the UFKW (Figure 14). This is the first detection of the UFKW in the equatorial electrojet. We emphasize that it is important to include measurements from multiple stations when UFKW signatures in the ionosphere are investigated using ground-based observations.

Acknowledgments

We thank the NASA Goddard Earth Sciences (GES) Data and Information Services Center (DISC) (https://disc.gsfc.nasa.gov/) for making the Aura/MLS geopotential height data (DOI: 10.5067/Aura/MLS/DATA2008) available. We also thank the European Space Agency (ESA) for providing the GOCE TEC data, which can be downloaded from https://eo-virtual-archive1.esa.int/GOCE_TEC.html. The GAIA simulations were performed using the computer system at the Research Institute for Information Technology of Kyushu University. The numerical data used in this study are available from GFZ Data Services (https://doi.org/10.5880/GFZ.2.3.2020.001). The GAIA simulations relied on the meteorological data provided from the Japanese 55-year Reanalysis (JRA-55) project carried out by the Japan Meteorological Agency (JMA). The magnetic data for Huancayo and Addis Ababa can be downloaded from the INTERMAGNET website (www.intermagnet.org). We thank Geophysical Institute of Peru, Addis Ababa University, and University of Paris for supporting the operation of magnetic field measurements at these observatories. The magnetic data for Tirunelveli can be downloaded from the website at the WDC Mumbai (https://wdciig.res.in). We thank the Director, Indian Institute of Geomagnetism (IIG), India for making the Tirunelveli data available. The Tatuoca magnetic data are accessible from GFZ Data Services (https://dataservices.gfz-potsdam.de/panmetaworks/showshort.php?id = escidoc:3504909). The magnetic data for Yap Island can be downloaded from the SuperMAG website (supermag.jhuapl.edu). The geomagnetic activity index *Kp* was provided by the GFZ German Research Centre for Geosciences (https://www.gfz-potsdam.de/en/kp-index/). The solar activity index $F_{10.7}$ was downloaded from the SPDF OMNIWeb database (https://omniweb.gsfc.nasa.gov). Wavelet software provided by C. Torrence and G. Compo is available at https://paos.colorado.edu/research/wavelets/. YY and YM was supported by the Deutsche Forschungsgemeinschaft (DFG) grant YA-574-3-1 and the Japan Society for the Promotion of Science (JSPS) grant, respectively, under the joint German-Japanese project. GBS was supported by Coordenação de Aperfeiçoamento de Pessoal de Nível Superior Brasil (CAPES) Finance Code 1799579 (PhD research grant).

References

Abdu, M. A., Brum, C. G., Batista, P. P., Gurubaran, S., Pancheva, D., Bageston, J. V., & Takahashi, H. (2015). Fast and ultrafast Kelvin wave modulations of the equatorial evening F region vertical drift and spread F development. *Earth, Planets and Space*, *67*(1), 1.

Acker, J. G., & Leptoukh, G. (2007). Online analysis enhances use of NASA earth science data. *Eos, Transactions American Geophysical Union*, *88*(2), 14–17.

Alken, P. (2020). Estimating currents and electric fields at low latitudes from satellite magnetic measurements. In *Ionospheric Multi-Spacecraft Analysis Tools* (pp. 233–254). Cham: Springer.

Chang, L. C., Palo, S. E., & Liu, H. L. (2011). Short-term variability in the migrating diurnal tide caused by interactions with the quasi 2 day wave. *Journal of Geophysical Research*, *116*, D12112. https://doi.org/10.1029/2010JD014996

Chang, L. C., Palo, S. E., Liu, H. L., Fang, T. W., & Lin, C. S. (2010). Response of the thermosphere and ionosphere to an ultra fast Kelvin wave. *Journal of Geophysical Research*, *115*, A00G04. https://doi.org/10.1029/2010JA015453

Chen, Y. W., & Miyahara, S. (2012). Analysis of fast and ultrafast Kelvin waves simulated by the Kyushu-GCM. *Journal of Atmospheric and Solar-Terrestrial Physics*, *80*, 1–11.

Chen, W. S., Pan, C., & Das, U. (2018). The mean zonal wind effect on the long-term variation of ultra-fast Kelvin waves in the mesosphere and lower thermosphere and in the upper stratosphere. *Journal of Atmospheric and Solar-Terrestrial Physics*, *179*, 459–467.

Cnossen, I., & Richmond, A. D. (2013). Changes in the Earth's magnetic field over the past century: Effects on the ionosphere-thermosphere system and solar quiet (Sq) magnetic variation. *Journal of Geophysical Research: Space Physics*, *118*, 849–858. https://doi.org/10.1029/2012JA018447

Davis, R. N., Chen, Y., Miyahara, S., & Mitchell, N. J. (2012). The climatology, propagation and excitation of ultra-fast Kelvin waves as observed by meteor radar, Aura MLS, TRMM and in the Kyushu-GCM. *Atmospheric Chemistry and Physics*, *12*(4), 1865–1879.

Egito, F., Buriti, R. A., Medeiros, A. F., & Takahashi, H. (2018). Ultrafast Kelvin waves in the MLT airglow and wind, and their interaction with the atmospheric tides. *Annales Geophysicae*, *36*, 231–241.

England, S. L., Liu, G., Zhou, Q., Immel, T. J., Kumar, K. K., & Ramkumar, G. (2012). On the signature of the quasi-3-day wave in the thermosphere during the January 2010 URSI World Day Campaign. *Journal of Geophysical Research*, *117*, A06304. https://doi.org/10.1029/2012JA017558

Fang, T. W., Akmaev, R., Fuller-Rowell, T., Wu, F., Maruyama, N., & Millward, G. (2013). Longitudinal and day-to-day variability in the ionosphere from lower atmosphere tidal forcing. *Geophysical Research Letters*, *40*, 2523–2528. https://doi.org/10.1002/grl.50550

Finlay, C. C., Olsen, N., Kotsiaros, S., Gillet, N., & Tøffner-Clausen, L. (2016). Recent geomagnetic secular variation from Swarm and ground observatories as estimated in the CHAOS-6 geomagnetic field model. *Earth, Planets and Space*, *68*(1), 112.

Forbes, J. M. (2000). Wave coupling between the lower and upper atmosphere: case study of an ultra-fast Kelvin wave. *Journal of Atmospheric and Solar-Terrestrial Physics*, *62*(17-18), 1603–1621.

Forbes, J. M., Zhang, X., Palo, S. E., Russell, J., Mertens, C. J., & Mlynczak, M. (2009). Kelvin waves in stratosphere, mesosphere and lower thermosphere temperatures as observed by TIMED/SABER during 2002–2006. *Earth, Planets and Space*, *61*(4), 447–453.

Gan, Q., Oberheide, J., & Pedatella, N. M. (2018). Sources, sinks, and propagation characteristics of the quasi 6-day wave and its impact on the residual mean circulation. *Journal of Geophysical Research: Atmospheres*, *123*, 9152–9170. https://doi.org/10.1029/2018JD028553

Gasperini, F., Forbes, J. M., Doornbos, E., & Bruinsma, S. (2015). Wave coupling between the lower and middle thermosphere as viewed from TIMED and GOCE. *Journal of Geophysical Research: Space Physics*, *120*, 5788–5804. https://doi.org/10.1002/2015JA021300

Gasperini, F., Forbes, J. M., Doornbos, E. N., & Bruinsma, S. L. (2018). Kelvin wave coupling from TIMED and GOCE: Inter/intra-annual variability and solar activity effects. *Journal of Atmospheric and Solar-Terrestrial Physics*, *171*, 176–187.

Gjerloev, J. (2012). The SuperMAG data processing technique. *Journal of Geophysical Research*, *117*, A09213. https://doi.org/10.1029/2012JA017683

Goncharenko, L., Chau, J., Condor, P., Coster, A., & Benkevitch, L. (2013). Ionospheric effects of sudden stratospheric warming during moderate-to-high solar activity: Case study of January 2013. *Geophysical Research Letters*, *40*, 4982–4986. https://doi.org/10.1002/grl.50980

Gu, S. Y., Dou, X., Lei, J., Li, T., Luan, X., Wan, W., & Russell, III J. (2014). Ionospheric response to the ultrafast Kelvin wave in the MLT region. *Journal of Geophysical Research: Space Physics*, *119*, 1369–1380. https://doi.org/10.1002/2013JA019086

Gu, S. Y., Dou, X. K., Yang, C. Y., Jia, M., Huang, K. M., Huang, C. M., & Zhang, S. D. (2018). Climatology and anomaly of the quasi-two-day wave behaviors during 2003–2018 austral summer periods. *Journal of Geophysical Research: Space Physics*, *124*, 544–556. https://doi.org/10.1029/2018JA026047

Gu, S. Y., Ruan, H., Yang, C. Y., Gan, Q., Dou, X., & Wang, N. (2018). The morphology of the 6-day wave in both the neutral atmosphere and F region ionosphere under solar minimum conditions. *Journal of Geophysical Research: Space Physics*, *123*, 4232–4240. https://doi.org/10.1029/2018JA025302

Gurubaran, S., Dhanya, R., Sathiskumar, S., & Patil, P. T. (2011). A case study of tidal and planetary wave coupling in the equatorial atmosphere-ionosphere system over India: preliminary results. In *Aeronomy of the Earth's Atmosphere and Ionosphere* (pp. 177–187). Dordrecht: Springer.

Hayashi, Y. (1971). A generalized method of resolving disturbances into progressive and retrogressive waves by space Fourier and time cross-spectral analyses. Journal of the Meteorological Society of Japan. Ser. II, *49*(2), 125–128.

Hirota, I. (1978). Equatorial waves in the upper stratosphere and mesosphere in relation to the semiannual oscillation of the zonal wind. *Journal of the Atmospheric Sciences*, *35*(4), 714–722.

Hirota, I. (1979). Kelvin waves in the equatorial middle atmosphere observed by the Nimbus 5. SCR. *Journal of the Atmospheric Sciences*, *36*(2), 217–222.

Holton, J. R., & Lindzen, R. S. (1968). A note on Kelvin waves in the atmosphere. *Monthly Weather Reviews*, *96*(6), 385–386.

Jarvis, M. (2006). Planetary wave trends in the lower thermosphere Evidence for 22-year solar modulation of the quasi 5-day wave. *Journal of Atmospheric and Solar-Terrestrial Physics*, *68*(17), 1902–1912.

Jin, H., Miyoshi, Y., Fujiwara, H., & Shinagawa, H. (2008). Electrodynamics of the formation of ionospheric wave number 4 longitudinal structure. *Journal of Geophysical Research*, *113*, A09307. https://doi.org/10.1029/2008JA013301

Jin, H., Miyoshi, Y., Fujiwara, H., Shinagawa, H., Terada, K., Terada, N., & Saito, A. (2011). Vertical connection from the tropospheric activities to the ionospheric longitudinal structure simulated by a new Earth's whole atmosphere-ionosphere coupled model. *Journal of Geophysical Research*, *116*, A01316. https://doi.org/10.1029/2010JA015925

Jin, H., Miyoshi, Y., Pancheva, D., Mukhtarov, P., Fujiwara, H., & Shinagawa, H. (2012). Response of migrating tides to the stratospheric sudden warming in 2009 and their effects on the ionosphere studied by a whole atmosphere-ionosphere model GAIA with COSMIC and TIMED/SABER observations. *Journal of Geophysical Research*, *117*, A10323. https://doi.org/10.1029/2012JA017650

Jonah, O. F., de Paula, E., Kherani, E., Dutra, S., & Paes, R. (2014). Atmospheric and ionospheric response to sudden stratospheric warming of January 2013. *Journal of Geophysical Research: Space Physics*, *119*, 4973–4980. https://doi.org/10.1002/2013JA019491

Kervalishvili, G., Xiong, C., Stolle, C., Rauberg, J., & van den IJsse, J. (2018). Computation of TEC and Rate of TEC Index (ROTI) from GOCE GPS (*GO-TN-HPF-GS-0337*). Paris, Île-de-France, France: ESA.

Kobayashi, S., Ota, Y., Harada, Y., Ebita, A., Moriya, M., Onoda, H., et al. (2015). The JRA-55 reanalysis: General specifications and basic characteristics. *Journal of the Meteorological Society of Japan. Ser. II*, *93*(1), 5–48.

Lieberman, R. S., & Riggin, D. (1997). High resolution Doppler imager observations of Kelvin waves in the equatorial mesosphere and lower thermosphere. *Journal of Geophysical Research*, *102*(D22), 26,117–26,130.
Liu, H. L. (2016). Variability and predictability of the space environment as related to lower atmosphere forcing. *Space Weather*, *14*, 634–658. https://doi.org/10.1002/2016SW001450
Liu, G., England, S. L., Immel, T. J., Kumar, K. K., Ramkumar, G., & Goncharenko, L. P. (2012). Signatures of the 3-day wave in the low-latitude and midlatitude ionosphere during the January 2010 URSI World Day campaign. *Journal of Geophysical Research*, *117*, A06305. https://doi.org/10.1029/2012JA017588
Liu, G., England, S. L., & Janches, D. (2019). Quasi two-, three-, and six-day planetary-scale wave oscillations in the upper atmosphere observed by TIMED/SABER over ~17 years during 2002–2018. *Journal of Geophysical Research: Space Physics*, *124*, 9462–9474. https://doi.org/10.1029/2019JA026918
Livesey, N., Read, W., Wagner, P., Froidevaux, L., Lambert, A., & Manney, G. (2017). Earth Observing System (EOS), Aura Microwave Limb Sounder (MLS), Version 4.2 x Level 2 data quality and description document, Version 4.2 x-3.0, D-33509. Jet Propulsion Laboratory, California Institute of Technology, Pasadena, California, available at: https://mls.jpl.nasa.gov/data/datadocs.php, last access, 7.
Love, J. J., & Chulliat, A. (2013). An international network of magnetic observatories. *Eos, Transactions American Geophysical Union*, *94*(42), 373–374.
Lühr, H., Xiong, C., Olsen, N., & Le, G. (2017). Near-Earth magnetic field effects of large-scale magnetospheric currents. *Space Science Reviews*, *206*(1-4), 521–545.
Matsuno, T. (1966). Quasi-geostrophic motions in the equatorial area. *Journal of the Meteorological Society of Japan. Ser. II*, *44*(1), 25–43.
Matzka, J., Siddiqui, T. A., Lilienkamp, H., Stolle, C., & Veliz, O. (2017). Quantifying solar flux and geomagnetic main field influence on the equatorial ionospheric current system at the geomagnetic observatory Huancayo. *Journal of Atmospheric and Solar-Terrestrial Physics*, *163*, 120–125.
Maute, A., Hagan, M., Yudin, V., Liu, H. L., & Yizengaw, E. (2015). Causes of the longitudinal differences in the equatorial vertical E×B drift during the 2013 SSW period as simulated by the TIME-GCM. *Journal of Geophysical Research: Space Physics*, *120*, 5117–5136. https://doi.org/10.1002/2015JA021126
Miyoshi, Y., & Fujiwara, H. (2003). Day-to-day variations of migrating diurnal tide simulated by a GCM from the ground surface to the exobase. *Geophysical research letters*, *30*(15), 1789. https://doi.org/10.1029/2003GL017695
Miyoshi, Y., & Fujiwara, H. (2006). Excitation mechanism of intraseasonal oscillation in the equatorial mesosphere and lower thermosphere. *Journal of Geophysical Research*, *111*, D14108. https://doi.org/10.1029/2005JD006993
Miyoshi, Y., Fujiwara, H., Jin, H., Shinagawa, H., Liu, H., & Terada, K. (2011). Model study on the formation of the equatorial mass density anomaly in the thermosphere. *Journal of Geophysical Research*, *116*, A05322. https://doi.org/10.1029/2010JA016315
Miyoshi, Y., Pancheva, D., Mukhtarov, P., Jin, H., Fujiwara, H., & Shinagawa, H. (2017). Excitation mechanism of non-migrating tides. *Journal of Atmospheric and Solar-Terrestrial Physics*, *156*, 24–36.
Morschhauser, A., Soares, G. B., Haseloff, J., Bronkalla, O., Protásio, J., Pinheiro, K., & Matzka, J. (2017). The magnetic observatory on Tatuoca, Belém, Brazil: History and recent developments. *Geoscientific Instrumentation, Methods and Data Systems*, *6*(2), 367.
Noja, M., Stolle, C., Park, J., & Lühr, H. (2013). Long-term analysis of ionospheric polar patches based on CHAMP TEC data. *Radio Science*, *48*(3), 289–301.
Nystrom, V., Gasperini, F., Forbes, J. M., & Hagan, M. E. (2018). Exploring wave-wave interactions in a general circulation model. *Journal of Geophysical Research: Space Physics*, *123*, 827–847. https://doi.org/10.1002/2017JA024984
Onogi, K., Tsutsui, J., Koide, H., Sakamoto, M., Kobayashi, S., Hatsushika, H., et al. (2007). The JRA-25 reanalysis. *Journal of the Meteorological Society of Japan. Ser. II*, *85*(3), 369–432.
Onohara, A., Batista, I., & Takahashi, H. (2013). The ultra-fast Kelvin waves in the equatorial ionosphere: Observations and modeling. *Annales Geophysicae*, *31*, 2.
Pancheva, D., Mitchell, N., & Younger, P. (2004). Meteor radar observations of atmospheric waves in the equatorial mesosphere/lower thermosphere over Ascension Island. In (Vol. 22, pp. 387–404).
Pancheva, D., Mukhtarov, P., Mitchell, N., Fritts, D., Riggin, D., Takahashi, H., & Ramkumar, G. (2008). Planetary wave coupling (5–6-day waves) in the low-latitude atmosphere–ionosphere system. *Journal of Atmospheric and Solar-Terrestrial Physics*, *70*(1), 101–122.
Pancheva, D., Mukhtarov, P., Shepherd, M., Mitchell, N., Fritts, D., Riggin, D., et al. (2006). Two-day wave coupling of the low-latitude atmosphere-ionosphere system. *Journal of Geophysical Research*, *111*, A07313. https://doi.org/10.1029/2005JA011562
Pancheva, D., Mukhtarov, P., & Siskind, D. E. (2018). Climatology of the quasi-2-day waves observed in the MLS/Aura measurements (2005–2014). *Journal of Atmospheric and Solar-Terrestrial Physics*, *171*, 210–224.
Pedatella, N., Liu, H. L., & Hagan, M. (2012). Day-to-day migrating and nonmigrating tidal variability due to the six-day planetary wave. *Journal of Geophysical Research*, *117*, A06301. https://doi.org/10.1029/2012JA017581
Phanikumar, D., Kumar, K. N., & Kumar, S. (2014). Signatures of ultra fast Kelvin waves in low latitude ionospheric TEC during January 2009 stratospheric warming event. *Journal of Atmospheric and Solar-Terrestrial Physics*, *117*, 48–53.
Ramkumar, T., Gurubaran, S., & Rajaram, R. (2009). Mesospheric planetary wave signatures in the equatorial electrojet. *Journal of Geophysical Research*, *114*, A03309. https://doi.org/10.1029/2007JA012935
Riggin, D. M., Fritts, D. C., Tsuda, T., Nakamura, T., & Vincent, R. A. (1997). Radar observations of a 3-day Kelvin wave in the equatorial mesosphere. *Journal of Geophysical Research*, *102*(D22), 26,141–26,157.
Salby, M. L., Hartmann, D. L., Bailey, P. L., & Gille, J. C. (1984). Evidence for equatorial Kelvin modes in Nimbus-7 LIMS. *Journal of the Atmospheric Sciences*, *41*(2), 220–235.
Sassi, F., Liu, H. L., Ma, J., & Garcia, R. R. (2013). The lower thermosphere during the Northern Hemisphere winter of 2009: A modeling study using high-altitude data assimilation products in WACCM-X. *Journal of Geophysical Research: Atmospheres*, *118*, 8954–8968. https://doi.org/10.1002/jgrd.50632
Schwartz, M., Lambert, A., Manney, G., Read, W., Livesey, N., Froidevaux, L., et al. (2008). Validation of the Aura Microwave Limb Sounder temperature and geopotential height measurements. *Journal of Geophysical Research*, *113*, D15S11. https://doi.org/10.1029/2007JD008783
Shinagawa, H. (2011). Ionosphere simulation. *Journal of NICT*, *56*(1-4), 199–207.
Siddiqui, T. A., Yamazaki, Y., Stolle, C., Lühr, H., Matzka, J., Maute, A., & Pedatella, N. (2018). Dependence of lunar tide of the equatorial electrojet on the wintertime polar vortex, solar flux, and QBO. *Geophysical Research Letters*, *45*, 3801–3810. https://doi.org/10.1029/2018GL077510

Soares, G., Matzka, J., & Pinheiro, K. (2018). Preliminary minute means geomagnetic observatory Tatuoca (TTB), 2008 to 2017. Retrieved from http://doi.org/10.5880/GFZ.2.3.2018.005

Soares, G., Yamazaki, Y., Matzka, J., Pinheiro, K., Morschhauser, A., Stolle, C., & Alken, P. (2018). Equatorial counter electrojet longitudinal and seasonal variability in the American sector. *Journal of Geophysical Research: Space Physics*, *123*, 9906–9920. https://doi.org/10.1029/2018JA025968

Sridharan, S., Gurubaran, S., & Rajaram, R. (2002). Radar observations of the 3.5-day ultra-fast Kelvin wave in the low-latitude mesopause region. *Journal of Atmospheric and Solar-Terrestrial Physics*, *64*(8-11), 1241–1250.

Stolle, C., Manoj, C., Lühr, H., Maus, S., & Alken, P. (2008). Estimating the daytime equatorial ionization anomaly strength from electric field proxies. *Journal of Geophysical Research*, *113*, A09310. https://doi.org/10.1029/2007JA012781

Takahashi, H., Wrasse, C., Fechine, J., Pancheva, D., Abdu, M., & Batista, I. (2007). Signatures of ultra fast Kelvin waves in the equatorial middle atmosphere and ionosphere. *Geophysical Research Letters*, *34*, L11108. https://doi.org/10.1029/2007GL029612

Takahashi, H., Wrasse, C., Pancheva, D., Abdu, M., Batista, I., Lima, L., & Shiokawa, K. (2006). Signatures of 3–6 day planetary waves in the equatorial mesosphere and ionosphere. *Annales Geophysicae*, *24*, 3343–3350.

Takeda, M. (1996). Effects of the strength of the geomagnetic main field strength on the dynamo action in the ionosphere. *Journal of Geophysical Research*, *101*(A4), 7875–7880.

Tapping, K. (2013). The 10.7 cm solar radio flux ($F_{10.7}$). *Space Weather*, *11*, 394–406. https://doi.org/10.1002/swe.20064

Teitelbaum, H., & Vial, F. (1991). On tidal variability induced by nonlinear interaction with planetary waves. *Journal of Geophysical Research*, *96*(A8), 14,169–14,178.

Torrence, C., & Compo, G. P. (1998). A practical guide to wavelet analysis. *Bulletin of the American Meteorological society*, *79*(1), 1–78.

Triplett, C. C., Immel, T. J., Wu, Y. J., & Cullens, C. (2019). Variations in the ionosphere-thermosphere system from tides, ultra-fast Kelvin waves, and their interactions. *Advances in Space Research*, *64*(10), 1841–1853.

Vincent, R. (1993). Long-period motions in the equatorial mesosphere. *Journal of Atmospheric and Terrestrial Physics*, *55*(7), 1067–1080.

Wallace, J. M., & Kousky, V. (1968). Observational evidence of Kelvin waves in the tropical stratosphere. *Journal of the Atmospheric Sciences*, *25*(5), 900–907.

Waters, J. W., Froidevaux, L., Harwood, R. S., Jarnot, R. F., Pickett, H. M., & Read, W. G. (2006). The earth observing system microwave limb sounder (EOS MLS) on the Aura satellite. *IEEE Transactions on Geoscience and Remote Sensing*, *44*(5), 1075–1092.

Xiong, C., Lühr, H., & Fejer, B. G. (2016). The response of equatorial electrojet, vertical plasma drift, and thermospheric zonal wind to enhanced solar wind input. *Journal of Geophysical Research: Space Physics*, *121*, 5653–5663. https://doi.org/10.1002/2015JA022133

Yamazaki, Y., & Kosch, M. J. (2015). The equatorial electrojet during geomagnetic storms and substorms. *Journal of Geophysical Research: Space Physics*, *120*, 2276–2287. https://doi.org/10.1002/2014JA020773

Yamazaki, Y., & Matthias, V. (2019). Large-amplitude quasi-10-day waves in the middle atmosphere during final warmings. *Journal of Geophysical Research: Atmospheres*, *124*, 9874–9892. https://doi.org/10.1029/2019JD030634

Yamazaki, Y., & Maute, A. (2017). Sq and EEJ A review on the daily variation of the geomagnetic field caused by ionospheric dynamo currents. *Space Science Reviews*, *206*(1-4), 299–405.

Yamazaki, Y., Richmond, A., Maute, A., Liu, H. L., Pedatella, N., & Sassi, F. (2014). On the day-to-day variation of the equatorial electrojet during quiet periods. *Journal of Geophysical Research: Space Physics*, *119*, 6966–6980. https://doi.org/10.1002/2014JA020243

Yamazaki, Y., Stolle, C., Matzka, J., & Alken, P. (2018). Quasi-6-day wave modulation of the equatorial electrojet. *Journal of Geophysical Research: Space Physics*, *123*, 4094–4109. https://doi.org/10.1029/2018JA025365

Yamazaki, Y., Stolle, C., Matzka, J., Liu, H., & Tao, C. (2018). Interannual variability of the daytime equatorial ionospheric electric field. *Journal of Geophysical Research: Space Physics*, *123*, 4241–4256. https://doi.org/10.1029/2017JA025165

Yiğit, E., & Medvedev, A. S. (2015). Internal wave coupling processes in Earths atmosphere. *Advances in Space Research*, *55*(4), 983–1003.

Yoshida, S., Tsuda, T., Shimizu, A., & Nakamura, T. (1999). Seasonal variations of 3.0 3.8-day ultra-fast Kelvin waves observed with a meteor wind radar and radiosonde in Indonesia. *Earth, Planets and Space*, *51*(7-8), 675–684.

Yue, J., Wang, W., Richmond, A. D., Liu, H. L., & Chang, L. C. (2013). Wavenumber broadening of the quasi 2 day planetary wave in the ionosphere. *Journal of Geophysical Research: Space Physics*, *118*, 3515–3526. https://doi.org/10.1002/jgra.50307

Yumoto, K., & the MAGDAS Group (2006). MAGDAS project and its application for space weather, *Solar influence on the heliosphere and Earth's environment: Recent progress and prospects* (pp. 309–405). Mumbai, India: Quest Publ.